

Title	Low-Temperature Synthesis of Nanostructured Zinc Oxide Films Using Inorganic/Organic Composites
Author(s)	Ueno, Naoyuki
Citation	大阪大学, 2013, 博士論文
Version Type	VoR
URL	https://hdl.handle.net/11094/27500
rights	
Note	

Osaka University Knowledge Archive : OUKA

<https://ir.library.osaka-u.ac.jp/>

Osaka University

Low-Temperature Synthesis of
Nanostructured Zinc Oxide Films Using
Inorganic/Organic Composites

Naoyuki UENO

March 2013

Low-Temperature Synthesis of Nanostructured Zinc Oxide Films Using Inorganic/Organic Composites

A dissertation submitted to
THE GRADUATE SCHOOL OF ENGINEERING SCIENCE
OSAKA UNIVERSITY

in partial fulfillment of the requirements for the degree of
DOCTOR OF PHILOSOPHY IN ENGINEERING

BY

Naoyuki UENO

March 2013

This thesis consists of five main chapters dealing with synthesis, modification and characterization of zinc oxide nanostructured films.

Chapter 1 covers a brief review of the properties of zinc oxide and recent progress in the research on the nanostructured zinc oxide. The objectives of this study are; (1) a synthesis of ordered zinc oxide nanostructure at low temperature and (2) a synthesis of zinc oxide with excellent optical and electrical properties. Inorganic/organic composites were used to achieve the objectives.

Chapters 2 and 3 focused on the synthesis of zinc oxide nanorods by using a zinc/sodium dodecyl sulfate (Zn/SDS) composite seed. The effects of growing condition over the morphologies of the zinc oxide nanorods were investigated by FE-SEM observations. Zinc oxide crystals were grown in the direction of *c*-axis perpendicular to the surface of the substrate. However, nucleation did not occur on a ZnAc₂ seed layer without SDS, indicating that the presence of the Zn/SDS seed enhanced the nucleation of ZnO crystals. Highly-dispersion of zinc in the composite effectively assists a nucleation of ZnO crystals. The results of X-ray absorption fine structure analyses suggest that ZnO crystals start to grow after an induction period of 20–30 min. The length and the aspect ratio of ZnO nanorods could be controlled by altering the molarity of ammonium and zinc nitrate in growth solutions. Besides, the stirring rate or supply of growth solution was helpful for further control of the morphology of ZnO nanorods.

Chapter 4 focused on the synthesis of zinc oxide nanosheet. The morphology of the zinc oxide was controlled with the difference by using various alcohols as a solvent. Sheet-like ZnO films were synthesized when ethanol was used as a solvent. The ZnO nanosheet films had higher transparency and conductivity than that of the ZnO nanorods. The thickness of the films was controlled from 450 nm to 5 μ m by altering a concentration of a zinc source in a growth solution. The sheet resistivity of the films decreased with an increase of the thickness. The films could be synthesized on a flexible substrate with high transparency which was more than 90% transmittance in visible light. Higher conductivity was obtained by doping the Al atoms in the ZnO nanosheet films.

In chapter 5, mesoporous zinc oxide films were synthesized by using triblock copolymer (Pluronic F127: EO₁₀₆PO₇₀EO₁₀₆) as a soft template agent. The relationships between the ratios of

Zn/F127, and the optical and electrical properties of the films were investigated by FE-SEM UV-vis spectra and XRD measurements. Mesoporous ZnO films calcined at 500°C showed a strong peak in the XRD pattern, showing a periodic distance of 12.8 nm. The visible light transmittance of the films was ranged from 50% to more than 90% by changing the Zn/EO molar ratio in precursor solutions. The electric resistivity of the films was decreased by doping the optimum amount of Al or B atom. The minimum value of the BZO film was 0.024 Ωcm which can be obtained at the atomic ratio of $\text{B/Zn} = 0.005$.

In chapter 6, the conclusions obtained in this research are summarized.

Contents

Chapter 1

General Introduction	1
1.1 Properties of ZnO	3
1.1.1 Crystal structures	3
1.1.2 Optical properties	6
1.2 Doping of ZnO	7
1.2.1 <i>n</i> -type doping	7
1.3 ZnO nanostructures	8
1.4 Synthesis of ZnO nanostructures	9
1.4.1 Physical techniques based approaches	9
1.4.2 Wet-chemical/solution based approaches	9
1.5 Applications	10
1.5.1 Transparent conductive oxide (TCO) for solar cell	10
1.6 Objective and outline of this thesis	12
1.6.1 Objective of this thesis	12
1.6.2 Outline of this thesis	13
References	15

Chapter 2

Low temperature synthesis of ZnO nanorods using a seed layer of zinc acetate/sodium dodecyl sulfate nanocomposite

2.1 Introduction	19
2.2 Experiment	21
2.2.1 ZnO Nanorods Synthesis by Hydrothermal Method	21
2.2.2 Characterization	21
2.3 Results and discussion	22
2.4 Conclusions	24
References	25

Chapter 3

Low-temperature synthesis of ZnO nanorods using organic-inorganic composite as a seed layer

3.1 Introduction	27
3.2 Experiment	29
3.2.1 Hydrothermal Synthesis of ZnO nanorods	29
3.2.2 Characterization	29
3.3 Results and discussion	30
3.3.1 Effect of the solution composition for seed layer on the growth of ZnO nanorods	30
3.3.2 Effect of solution composition on the growth of ZnO nanorods	33
3.3.3 Effect of handling of solution on the growth of ZnO nanorods	37
3.4 Conclusions	39
References	40

Chapter 4

Low-temperature hydrothermal synthesis of ZnO nanosheet using organic/inorganic composite as seed layer

4.1 Introduction	43
4.2 Experiment	44
4.2.1 Synthesis of ZnO nanosheet	44
4.2.2 Characterizations	45
4.3 Results and Discussion	45
4.4 Conclusion	49
References	50

Chapter 5

Synthesis of mesoporous ZnO, AZO, and BZO transparent conducting films using nonionic triblock copolymer as template

5.1 Introduction	51
5.2 Experiment	52
5.2.1 Synthesis of mesoporous ZnO films	52

5.2.2 Characterization	53
5.3 Results and Discussion	54
5.4 Conclusion	57
References	58

Chapter 6

Summary

6.1 Summary	59
6.1.1 Synthesis of Zinc Oxide Nanorods Films using Zn/SDS Composite	59
6.1.2 Formation Mechanism and Control of Zinc Oxide Nanorods Films	60
6.1.3 Synthesis of Zinc Oxide Nanosheet Films using Zn/SDS Composite	60
6.1.4 Synthesis of Porous Zinc Oxide Films using Zn/F127 Composite	60

List of Publications	61
-----------------------------	----

Acknowledgements	63
-------------------------	----

Chapter 1

General Introduction

There has been a great deal of interest in zinc oxide (ZnO) semiconductor materials lately, as seen from a surge of a relevant number of publications. The interest in ZnO is fueled and fanned by its prospects in optoelectronics applications owing to its direct wide band gap ($E_g \sim 3.3$ eV at 300 K). Some optoelectronic applications of ZnO overlap with that of GaN, another wide-gap semiconductor ($E_g \sim 3.4$ eV at 300 K) which is widely used for production of green, blue-ultraviolet, and white light-emitting devices. However, ZnO has some advantages over GaN among which are the availability of fairly high-quality ZnO bulk single crystals and a large exciton binding energy (~ 60 meV). ZnO is not really a newly discovered material. Research on ZnO has continued for many decades with interest following a roller-coaster pattern. In terms of its characterization, reports go back to 1935 or even earlier. For example, lattice parameters of ZnO were investigated for many decades.[1,2] Similarly, optical properties and processes in ZnO as well as its refractive index were extensively studied many decades ago.[3–5] Vibrational properties by techniques such as Raman scattering were also determined early on.[6] Investigations of ZnO properties presumes that ZnO samples were available. Growth methods not much different from what is employed lately have been explored, among which are chemical-vapor transport,[7] vapor-phase growth,[8] hydrothermal growth[9]. The ZnO bulk crystals have been grown by a number of methods, and large-size ZnO substrates are available.[10] High-quality ZnO films can be grown at relatively low temperatures (less than 700 °C). The large exciton binding energy of ~ 60 meV paves the way for an intense near-band-edge excitonic emission at room and higher temperatures, because this value is 2.4 times that of the room-temperature (RT) thermal energy ($k_B T = 25$ meV). There have also been a number of reports on laser emission from ZnO-based structures at RT and beyond. It should be

noted that besides the above-mentioned properties of ZnO, there are additional properties which make it preferable over other wide-band-gap materials: its high-energy radiation stability and amenability to wet chemical etching.[11] ZnO is easily etched in all acids and alkalis, and this provides an opportunity for fabrication of small-size devices. In addition, ZnO has the same crystal structure and close lattice parameters to that of GaN and as a result can be used as a substrate for epitaxial growth of high-quality GaN films.[12]

ZnO has recently found other niche applications as well, such as fabrication of transparent thin-film transistors, where the protective covering preventing light exposure is eliminated since ZnO-based transistors are insensitive to visible light. Also up to $2 \times 10^{21} \text{ cm}^{-3}$ charge carriers can be introduced by heavy substitutional doping into ZnO. By controlling the doping level electrical properties can be changed from insulator through *n*-type semiconductor to metal while maintaining optical transparency that makes it useful for transparent electrodes in flat-panel displays and solar cells.

However, in spite of many decades of investigations, some of the basic properties of ZnO still remain unclear. For example, the nature of the residual *n*-type conductivity in undoped ZnO films, whether being due to impurities of some native defect or defects, is still under some degree of debate. Some authors ascribe the residual background to intrinsic defects [oxygen vacancies (V_O) and interstitial zinc atoms (Zn_i),] and others to uncontrollable hydrogen impurities introduced during growth. The well-known green band in ZnO luminescence spectra (manifesting itself as a broad peak around 500–530 nm), observed nearly in all samples regardless of growth conditions, is related to singly ionized oxygen vacancies by some and to residual copper impurities by others. Simply, a requisite consensus is lacking.

While *p*-type ZnO is difficult to attain, the advantages of ZnO are being explored and exploited by alternative methods such as heteroepitaxy in which *p-n* heterostructures can be obtained by depositing *n*-type ZnO films on other *p*-type materials while still utilizing ZnO as the active layer. Progress has been made in this arena with a number of heterostructures fabricated wherein one of the following, Si, NiO, GaN, AlGaN, SiC, ZnTe, CuO, CdTe, etc., plays the role of *p*-type layer. These results are just harbingers of what can be expected of ZnO in an effort to position it for future device applications. As in the early developments of GaN predating the demonstration of *p*-type conductivity, metal-insulator-semiconductor device structures not requiring *p*-type ZnO have been introduced but lack the high efficiency.

1.1 Properties of ZnO

1.1.1 Crystal structures

Most of the group-II-VI binary compound semiconductors crystallize in either cubic zinc-blende or hexagonal wurtzite structure where each anion is surrounded by four cations at the corners of a tetrahedron, and vice versa. This tetrahedral coordination is typical of sp^3 covalent bonding, but these materials also have a substantial ionic character. ZnO is a II-VI compound semiconductor whose ionicity resides at the borderline between covalent and ionic semiconductor. The crystal structures shared by ZnO are wurtzite (B4), zinc blende (B3), and rocksalt (B1), as schematically shown in **Fig. 1.1**. At ambient conditions, the thermodynamically stable phase is wurtzite. The zinc-blende ZnO structure can be stabilized only by growth on cubic substrates, and the rocksalt (NaCl) structure may be obtained at relatively high pressures.

The wurtzite structure has a hexagonal unit cell with two lattice parameters, a and c , in the ratio of $c/a = \sqrt{8/3} = 1.633$ and belongs to the space group of C_{6v}^4 or $P6_3mc$. A schematic representation of the wurtzitic ZnO structure is shown in **Fig. 1.2**. The structure is composed of two interpenetrating hexagonal-close-packed (hcp) sublattices, each of which consists of one type of atom displaced with respect to each other along the threefold c -axis by the amount of $u = 3/8 = 0.375$ (in an ideal wurtzite structure) in fractional coordinates (the u parameter is defined as the

length of the bond parallel to the c axis, in units of c). Each sublattice includes four atoms per unit cell and every atom of one kind (group-II atom) is surrounded by four atoms of the other kind (group VI), or vice versa, which are coordinated at the edges of a tetrahedron. In a real ZnO crystal, the wurtzite

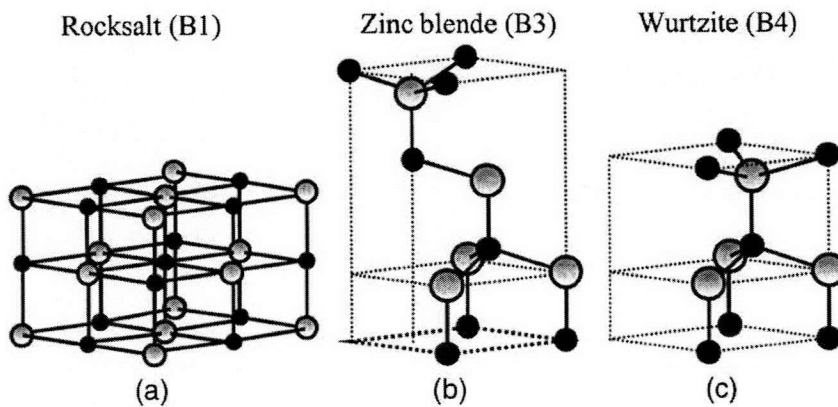


Fig. 1.1 Stick and ball representation of ZnO crystal structures: (a) cubic rocksalt (B1), (b) cubic zinc blende (B3), and (c) hexagonal wurtzite (B4). The shaded gray and black spheres denote Zn and O atoms, respectively.

structure deviates from the ideal arrangement, by changing the c/a ratio or the u value. It should be pointed out that a strong correlation exists between the c/a ratio and the u parameter in that when the c/a ratio decreases, the u parameter increases in such a way that those four tetrahedral distances remain nearly constant through a distortion of tetrahedral angles due to long-range polar interactions. These two slightly different bond lengths will be equal if the following relation holds:

$$u = \left(\frac{1}{3}\right)\left(\frac{a^2}{c^2}\right) + \frac{1}{4}$$

Since the c/a ratio also correlates with the difference of the electronegativities of the two constituents, components with the greatest differences show the largest departure from the ideal c/a ratio.[13] Like other II-VI semiconductors, wurtzite ZnO can be transformed to the rocksalt (NaCl) structure at relatively modest external hydrostatic pressures. The reason for this is that the reduction of the lattice dimensions causes the interionic Coulomb interaction to favor the ionicity more over the covalent nature. The space-group symmetry of the rocksalt type of structure is $Fm\bar{3}m$, and the structure is sixfold coordinated. However, the rocksalt structure cannot be stabilized by the epitaxial growth. In ZnO, the pressure-induced phase transition from the wurtzite (B4) to the rocksalt (B1) phase occurs at approximately 10 GPa and a large volume decrease of about 17%, as reported by Bates *et al.*[14] They found that high-pressure cubic phase is metastable for long periods of time even at ambient pressure and above 100°C. More recently, energy-dispersive X-ray diffraction (EDXD) using synchrotron radiation has been employed to probe the phase transition in ZnO.[15,16] Gerward and Olsen[15] and Recio *et al.*[16] observed that the hexagonal wurtzite structure of ZnO undergoes a structural phase transformation with a transition pressure $p_{tr} = 10$ GPa and completed at about 15 GPa. Accordingly, a large fraction of

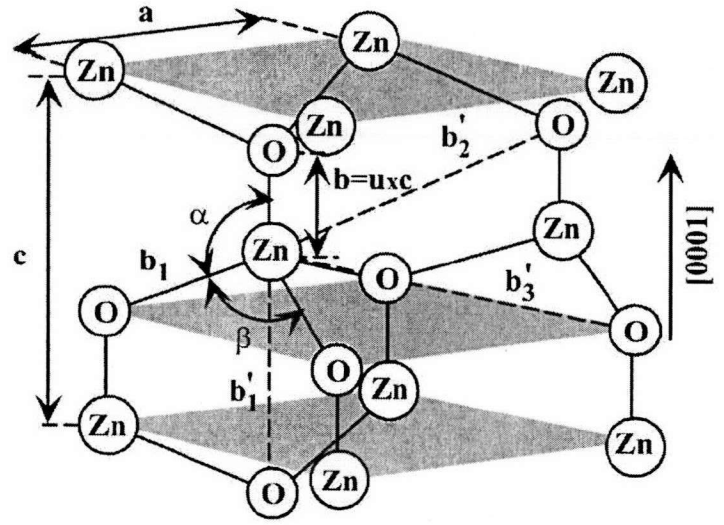


Fig. 1.2 Schematic representation of a wurtzitic ZnO structure having lattice constants a in the basal plane and c in the basal direction; u parameter is expressed as the bond length or the nearest-neighbor distance b divided by c (0.375 in ideal crystal), and α and β (109.47° in ideal crystal) are the bond angles.

the B1 phase is retained when the pressure is released, indicating the metastable state of the rocksalt phase of ZnO even at zero pressure.

In contrast, using *in situ* x-ray diffraction, Jamieson[17] and later, using EDXD, Desgreniers[18] reported that this transition is reversible at room temperature. A large number of EDXD spectra were recorded at pressures ranging from 0.1 MPa to 56 ± 1 GPa at room temperature with increasing and decreasing pressures. A clear wurtzite-to-rocksalt transition was observed starting at 9.1 ± 0.2 GPa with increasing pressure. The structural transition is completed at 9.6 GPa, resulting in a 16.7% change in the unit-cell volume. Upon decompression, it was observed that ZnO reverts to the wurtzite structure at 1.9 ± 0.2 GPa, below which a single phase is present. The phase hysteresis is consequently substantial. Similar hysteresis was also reported by Karzel *et al.*[19] for this transition from x-ray and Zn- Mössbauer spectroscopy studies. The transition pressure was measured to be 8.7 GPa for increasing pressure, whereas it was 2.0 GPa for decreasing pressure.

Because of the tetrahedral coordination of wurtzite and zinc-blende structures, the four nearest neighbors and 12 next-nearest neighbors have the same bond distance in both structures. Stick and ball stacking models for *2H* wurtzitic and *3C* zinc-blende polytypes of ZnO crystals are shown in **Fig. 1.1** The main difference between these two structures lies in the stacking sequence of closed-packed diatomic planes. The wurtzite structure consists of triangularly arranged alternating biatomic close-packed (0001) planes, for example, Zn and O pairs, thus the stacking sequence of the (0001) plane is *AaBbAaBb...* in the $\langle 0001 \rangle$ direction. In contrast, the zincblende structure consists of triangularly arranged atoms in the closed-packed (111) planes along the $\langle 111 \rangle$ direction that causes a stacking order of *AaBbCcAaBbCc....* The small and large letters stand for the two different kinds of constituents.

Since none of the three structures described above possess an inversion symmetry, the crystal exhibits crystallographic polarity, which indicates the direction of the bonds, i.e., closed-packed (111) planes in zinc-blende and rocksalt structures and corresponding (0001) basal planes in the wurtzite structure differ from $(\overline{111})$ and $(000\overline{1})$ planes, respectively. The convention is that the [0001] axis points from the face of the O plane to the Zn plane and is the positive *z* direction. In other words, when the bonds along the *c* direction are from cation (Zn) to anion (O), the polarity is referred to as Zn polarity. By the same argument, when the bonds along the *c* direction are from anion (O) to cation (Zn), the polarity is referred to as O polarity. Many properties of the material

depend also on its polarity, for example, growth, etching, defect generation and plasticity, spontaneous polarization, and piezoelectricity. In wurtzite ZnO, besides the primary polar plane (0001) and associated direction $\langle 0001 \rangle$, which are the most commonly used surface and direction for growth, many other secondary planes and directions exist in the crystal structure.

1.1.2 Optical properties

The optical properties of a semiconductor are connected with both intrinsic and extrinsic effects. Intrinsic optical transitions take place between the electrons in the conduction band and holes in the valence band, including excitonic effects due to the Coulomb interaction. Excitons are classified into free and bound excitons. In high-quality samples with low impurity concentrations, the free exciton can also exhibit excited states, in addition to their ground-state transitions. Extrinsic properties are related to dopants or defects, which usually create discrete electronic states in the band gap, and therefore influence both optical-absorption and emission processes. The electronic states of the bound excitons (Bes) depend strongly on the semiconductor material, in particular, the band structure. In theory, excitons could be bound to neutral or charged donors and acceptors. A basic assumption in the description of the principal bound-exciton states for neutral donors and acceptors is a dominant coupling of the like particles in the BE states. For a shallow neutral-donorbound exciton (DBE), for example, the two electrons in the BE state are assumed to pair off into a two-electron state with zero spin. The additional hole is then weakly bound in the net hole-attractive Coulomb potential set up by this bound two-electron aggregate. Similarly, shallow-neutral acceptor-bound excitons (ABEs) are expected to have a two hole state derived from the topmost valence band and one electron interaction. These two classes of bound excitons are by far the most important cases. Other defect-related transitions could be seen in optical spectra such as free to bound electron-acceptor, bound to bound (donor-acceptor), and the so-called yellow/green luminescence.

1.2 Doping of ZnO

ZnO has a strong potential for various short-wavelength optoelectronic device applications. In order to attain the potential offered by ZnO, both high-quality *n*- and *p*-type ZnO are indispensable. However, difficulty in bipolar carrier doping (both *n*- and *p*- types) is a major obstacle as seen in other wide-band-gap semiconductors such as GaN and II-VI compound semiconductors including ZnS, ZnSe, and ZnTe.[20,21] Unipolar doping has not been a surprising issue in wide-band-gap semiconductors: ZnO, GaN, ZnS, and ZnSe are easily doped to *n*-type, while *p*-type doping is difficult.

1.2.1 *n*-type doping

ZnO with a wurtzite structure is naturally an *n*-type semiconductor because of a deviation from stoichiometry due to the presence of intrinsic defects such as O vacancies (V_O) and Zn interstitials (Zn_i). Undoped ZnO shows intrinsic *n*-type conductivity with very high electron densities of about 10^{21} cm^{-3} . [21] Although it is experimentally known that unintentionally doped ZnO is *n* type, whether the donors are Zn_i and V_O is still controversial. The first-principles study suggested that none of the native defects show high-concentration shallow donor characteristics.[22] However, Look et al.[23] suggested that Zn_i rather than V_O is the dominant native shallow donor in ZnO with an ionization energy of about 30–50 meV. It has also been suggested that the *n*-type conductivity of unintentionally doped ZnO films is only due to hydrogen (H) acts as a shallow donor with an ionization energy about 30 meV. [22,24,25] This assumption is valid since hydrogen is always present in all growth methods and can easily diffuse into ZnO in large amounts due to its large mobility. First-principles calculations also suggested that unintentionally incorporated hydrogen acts as a source of conductivity and behaves as a shallow donor in ZnO.[26]

n-type doping of ZnO is relatively easy compared to *p*-type doping. Group-III elements Al, Ga, and In as substitutional elements for Zn and group-VII elements Cl and I as substitutional elements for O can be used as *n*-type dopants.[27] Doping with Al, Ga, and In has been attempted by many groups, resulting in high-quality, highly conductive *n*-type ZnO films.[28-31] Myong *et*

al.[28] grew Al-doped ZnO films by photoassisted MOCVD method and obtained highly conductive films with a minimum resistivity of $6.2 \times 10^{-4} \Omega \text{ cm}$. Ataev *et al.*[29] reported resistivities as low as $1.2 \times 10^{-4} \Omega \text{ cm}$ for Ga-doped ZnO films grown by chemical-vapor deposition. Ko *et al.*[31] also succeeded in Ga doping of ZnO films grown on GaN templates by plasmaassisted MBE. Thus, *n*-type doping of ZnO is developed very well. Such films are successfully used in various applications as *n*-type layers in light-emitting diodes as well as transparent Ohmic contacts.

1.3 ZnO nanostructures

One-dimensional semiconductor nanowires and nanorods have attracted increasing attention due to their physical properties arising from quantum confinement such as electronic quantum transport and enhanced radiative recombination of carriers. Nanowires have promising potentials in extensive applications and are the fundamental building blocks for fabricating short-wavelength nanolasers, field-effect transistors, ultrasensitive nanosized gas sensors, nanoresonators, transducers, actuators, nanocantilevers, and field emitters (Fes).[32,33] These nanostructures are the ideal systems for studying transport mechanisms in one-dimensional (1D) systems, which are of benefit not only for understanding the fundamental phenomena in low-dimensional systems but also for developing new generation nanodevices with high performance. Many nanowires made of materials such as Si, C, InP, GaAs, CdS, SnO₂, GaN, ZnO, and In₂O₃ have been fabricated for different applications using mostly a catalystassisted vapor-liquid-solid (VLS) growth method (solid vapor process).[32,34,35] Among these materials ZnO is considered to be the most prospective one due to its large exciton binding energy (60 meV), high electromechanical coupling constant, and resistivity to harsh environment. Therefore, 1D ZnO structures stimulated so much attention, and a large number of publications have appeared lately reporting nanostructures of various shapes (nanowires, nanobelts, nanorings, nanotubes, nanodonuts, nanopropellers, etc.) grown by different methods.[32,34-36] The growth of patterned and aligned one-dimensional nanostructures is important for device applications.

1.4 Synthesis of ZnO nanostructures

1.4.1 Physical techniques based approaches

The physical and chemical properties of nanomaterials vary as a function of size, shape and surface chemistry. Thus, new synthetic strategies are vital for the development of novel nanomaterials. Generally, the synthesis methods for ZnO nanostructures can be divided into two groups: wet-chemical/solution based and physical techniques based [37]. Physical techniques, such as vapor–liquid–solid (VLS), vapor solid and chemical vapor deposition (CVD) in addition to thermal evaporation, typically require high temperatures and pressures as well as particular substrates and result in low product yield. These methods produce highquality ZnO nanostructures; however, the methods are energy and cost intensive. Wet-chemical/solution based methods include hydrothermal/solvothermal processes, solution–liquid–solid (SLS) and capping agents/surfactant-assisted synthesis. Zinc readily forms hydroxy and ammonia complexes and these methods are based on the hydrolysis of such complexes at elevated or room temperatures. Further, the growth direction can be controlled with various additives in these methods. Amine compounds are often used to direct growth in the *c*-direction, whereas citrate inhibits *c*-direction growth and directs the crystal shape into thicker rods or even plates. Thus, wet-chemical/solution based methods provide convenient, facile manipulation, potential for scale-up and a lower temperature pathway for the fabrication of the desired ZnO nanostructures [37-39]. Among these methods, the solution based method via seed layer deposition followed by ZnO growth is the most common procedure for growing nanostructures. Recently, electrochemical techniques have also emerged as a new synthesis method for ZnO nanostructures [38,40].

1.4.2 Wet-chemical/solution based approaches

The solutions based approach has gained much interest compared to other techniques for ZnO nanostructure growth. In this approach, morphological and structural characteristics of the grown ZnO nanostructures can be controlled by adjusting the growth process parameters, such as the reagent of interest, stoichiometry, temperature and pH [41,42]. Further, alcohol molecules, such as

those in ethanolamine family (growth-directing), or stabilizing solvents play the vital role of contributing unoccupied oxygen to Zn^{2+} to form ZnO [43]. Using different amine precursors and surfactant-free hydrothermal processes various controllable ZnO architectures, such as flower-like structures radially assembled by rods, nails or towers and radialized bundled tubular structures can be synthesized. The different morphologies of ZnO could be obtained using different amine sources, where different hydroxyl ion releasing rates and their preferential adsorption contribute to different reaction rates and hence play a crucial role in controlling the assembly of different ZnO architectures [44]. Investigation related to the influence of parameters such as pH, concentration, time and growth temperature on the morphological control of ZnO nanostructures reveal that pH plays a crucial role in dictating the nano-morphologies [45]. Further, nanotetrapod-like, flowerlike and urchin-like ZnO nanostructures can be obtained at higher pH values (≥ 8), whereas rod-like structures can be obtained at lower pH values. Changes in concentrations result in changes in size and shape of nanostructures whereas, the growth temperature influence the aspect ratio of nanostructure [45]. The most common precursor used for ZnO nanostructure growth includes zinc nitrate ($\text{Zn}(\text{NO}_3)_2$) [46,47], zinc powder (Zn) [48], zinc chloride (ZnCl_2) [49], zinc acetate ($\text{Zn}(\text{CH}_3\text{COO})_2$) [50] and zinc sulfate (ZnSO_4) [51], with growth-orienting reagents such as hexamethylenetetramine (HMTA) [34], ammonia (NH_3) [40], citric acid [53], ascorbic acid [54] and sodium hydroxide (NaOH) [55]. A great number of wet chemical/solution approaches used for the synthesis of ZnO nanostructures have been documented in the last few years, many of which involve the deposition of a seed layer on a base matrix, which is subsequently utilized for nanostructure growth. A seed layer on base matrix from a seeding solution can be prepared by dipping [47], thermal decomposition [56], thermal evaporation [48], sputtering [57] or a sol-gel method [46].

1.5 Applications

1.5.1 Transparent conductive oxide (TCO) for solar cell

ZnO with an electron affinity of 4.35 eV and a direct band gap energy of 3.28 eV is typically an n-type semiconductor material with the residual electron concentration of $\sim 10^{17} \text{ cm}^{-3}$ [58].

However, the doped ZnO films have been realized with very attractive electrical and optical properties for electrode applications. The dopants that have been used for the ZnO-based binary TCOs are Ga, Al, B, In, Y, Sc, V, Si, Ge, Ti, Zr, Hf, and F [59]. Among the advantages of the ZnO-based TCOs are low cost, abundant material resources, and non-toxicity [60]. At present, ZnO heavily doped with Ga and Al (dubbed GZO and AZO) has been demonstrated to have low resistivity and high transparency in the visible spectral range and, in some cases, even outperform ITO and FTO. The dopant concentration in GZO or AZO is more often in the range of 10^{20} – 10^{21} cm⁻³ and in GZO typical reported mobility is near or slightly below 50 cm²/V s [61]. Ionization energies of Al and Ga donors (in the dilute limit which decreases with increased doping) are 53 and 55 meV, respectively, which are slightly lower than that of In (63 meV) [62]. Agura *et al.* [63] reported a very low resistivity of $\sim 8.5 \times 10^{-5}$ Ωcm for AZO, and Park *et al.* reported a resistivity of $\sim 8.1 \times 10^{-5}$ Ωcm for GZO [64], both of which are similar to the lowest reported resistivity of $\sim 7.7 \times 10^{-5}$ Ωcm for ITO [65]. The typical transmittance of AZO and GZO is easily 90% or higher, [66] which is comparable to the best value reported for ITO when optimized for transparency alone and far exceeds that of the traditional semitransparent and thin Ni/Au metal electrodes with transmittance below 70% in the visible range [67]. The high transparency of AZO and GZO originates from the wide band gap nature of ZnO [68]. Low growth temperature of AZO or GZO also intrigued researchers with respect to transparent electrode applications in solar cells [69]. As compared to ITO, ZnO-based TCOs show better thermal stability of resistivity [70] and better chemical stability at higher temperatures [71], both of which bode well for the optoelectronic devices in which this material would be used. In short, AZO and GZO are the TCOs attracting more attention, for replacing ITO. From the cost and availability and environmental points of view, AZO appears to be the best candidate. This conclusion is also bolstered by batch process availability for large-area and large-scale production of AZO.

B-doped ZnO has been reported to exhibit a lateral laser-induced photovoltage (LPV), which is expected to make it a candidate for position-sensitive photodetectors [72]. In-doped ZnO prepared by pulsed laser deposition and spray pyrolysis is discussed in Refs. [73], respectively. Y-doped ZnO deposited by sol-gel method on silica glass has been reported in Ref. [74]. Ilican *et al.* [75] reported on the structural, optical and electrical properties of F-doped ZnO formed by the sol-gel process and also listed almost all the relevant activities in the field. For drawing the contrast, we should reiterate that among all the dopants for ZnO-based binary TCOs, Ga and Al are thought to

be the best candidates so far.

The above-mentioned ZnO-based TCOs have relatively large refractive indices as well, in the range of 1.9–2.2, which are comparable to those of ITO [76] and FTO [77]. For comparison, the refractive indices of commercial ITO/glass decrease from 1.9 at wavelength of 400 nm to 1.5 at a wavelength of 800 nm [76]. The high refractive indices reduce internal reflections and allow employment of textured structures in LEDs to enhance light extraction beyond that made feasible by enhanced transparency alone [70]. The dispersion in published values of the refractive index is attributed to variations in properties of the films prepared by different deposition techniques. For example, amorphous ITO has lower refractive index than textured ITO. It is interesting to note that nanostructures such as nanorods [78] and nanotips [79] as well as controllable surface roughness [80] could enhance light extraction/absorption in LEDs and solar cells, thus improving device performance. Fortunately, such nanostructures can be easily achieved in ZnO by choosing and controlling the growth conditions.

The averaged resistivity of ITO by different techniques is $\sim 1 \times 10^{-4} \Omega\text{cm}$, which is much higher than that of FTO. For FTO, the typically employed technique is spray pyrolysis which can produce the lowest resistivity of $\sim 3.8 \times 10^{-4} \Omega\text{cm}$. For AZO/GZO, the resistivities listed here are comparable to or slightly higher than ITO but their transmittance is slightly higher than that of ITO. Obviously, AZO and GZO as well as other ZnO-based TCOs are promising to replace ITO for transparent electrode applications in terms of their electrical and optical properties. Klaus Ellmer et al. have provided a decent work regarding the use of ZnO transparent conductive electrode in thin film solar cells with much more details including the chemical, structural, optical, electrical, and interface properties of ZnO, which is a useful reference for the related field workers [81].

1.6 Objective and outline of this thesis

1.6.1 Objective of this thesis

Zinc oxide have shown many advantages in practical application especially in the field of optoelectronics. However, the economical advantage of zinc oxide is not utilized because the

synthesis method to get high performance zinc oxide is expensive as well as other materials. The purpose of this study is to establish the synthesis and morphological control of nanostructured zinc oxide films at low temperature and to clarify of the mechanism of growth of zinc oxide under such condition.

The inorganic/organic composite was used for accomplishing the low temperature synthesis of the films. Such composite was employed so far to synthesis mesoporous silica[82], mesoporous carbon[83] films. Ogawa prepared a continuous surfactant-silicate mesostructured film by solvent evaporation using spin-coating (**Fig. 1.3**) [82, 84]. In this work, partially hydrolyzed tetramethoxysilane in acid condition and an alkyltrimethylammonium bromide were mixed and the solution coated on to a substrate. Transparent thin films were formed on the substrate with the thickness controlled by spin rate. These films showed a layered structure organized parallel to the substrate. The spin-coated films are shown to retain ordered structures by X-ray diffraction patterns and to have high surface areas after calcination. Ogawa et al. have also published syntheses of transparent cubic and hexagonal films produced by varying the inorganic/surfactant molar ratios. These films were about 1 μm thick on glass substrates and did not crack or peel off the substrate after calcination.

Inorganic/organic composite has ordered nanostructure and dispersibility of inorganic species. The objective of this study is to develop new methods to synthesize and control zinc oxide nanostructures using such advantages of the inorganic/organic structure.

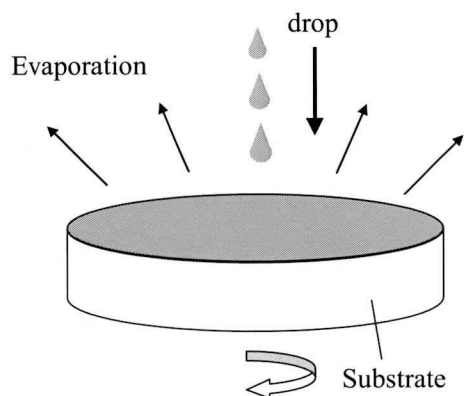


Fig. 1.3 Schematic illustration of solvent evaporation method using spin-coating

1.6.2 Outline of this thesis

Chapters 2 and 3 deal with a synthesis of zinc oxide nanorods using a zinc acetate/ sodium dodecyl sulfate (ZnAc_2/SDS) composite as a seed layer. The seed layer was hydrothermally grown. The effect of the composite and conditions of growth reaction was investigated. Morphological changes of the nanorods were studied by FE-SEM observation.

The morphology of zinc oxide should be controlled to improve transparency and conductivity of the films. In chapter 4, a synthesis method of transparent zinc oxide nanosheet was developed.

The zinc oxide with a new morphology was synthesized by controlling the nucleation and kinetics of growth reaction of zinc oxide.

In chapter 5, mesopores was introduced to zinc oxide films in order to improve conductivity. The mesostructure of the films is formed by a self-assembly of organic-inorganic composites. The mesopores are generated by the thermal decomposition of organic species. The transparency and conductivity of the zinc oxide was measured and the effects of the morphology were investigated.

References

- [1] R. B. Heller, J. McGannon, and A. H. Weber, *J. Appl. Phys.* 21 (1950) 1283.
- [2] G. P. Mohatny and L. V. Azaroff, *J. Chem. Phys.* 35 (1961) 1268.
- [3] Y. S. Park, C. W. Litton, T. C. Collins, and D. C. Reynolds, *Phys. Rev.* 143 (1965) 512.
- [4] E. Mollwo, *Z. Angew. Phys.* 6 (1954) 257.
- [5] J. L. Freeouf, *Phys. Rev. B* 7 (1973) 3810.
- [6] M. Tsuboi and A. Wada, *J. Chem. Phys.* 48 (1968) 2615.
- [7] G. Galli and J. E. Coker, *Appl. Phys. Lett.* 16 (1970) 439.
- [8] M. Shiloh and J. Gutman, *J. Cryst. Growth* 11 (1971) 105.
- [9] D. F. Croxall, R. C. C. Ward, C. A. Wallace, and R. C. Kell, *J. Cryst. Growth* 22 (1974) 117.
- [10] E. Ohshima, H. Ogino, I. Niikura, K. Maeda, M. Sato, M. Ito, and T. Fukuda, *J. Cryst. Growth* 260 (2004) 166.
- [11] D. C. Look, *Mater. Sci. Eng. B* 80 (2001) 381.
- [12] X. Gu, M. A. Reshchikov, A. Teke, D. Johnstone, H. Morkoc, B. Nemeth, and J. Nause, *Appl. Phys. Lett.* 84, 2268 _2004_; *J. Mater. Sci.* 15 (2004) 373.
- [13] E. Kisi and M. M. Elcombe, *Acta Crystallogr., Sect. C: Cryst. Struct. Commun.* C 45 (1989) 1867.
- [14] C. H. Bates, W. B. White, and R. Roy, *Science* 137 (1962) 993.
- [15] L. Gerward and J. S. Olsen, *J. Synchrotron Radiat.* 2 (1995) 233.
- [16] J. M. Recio, M. A. Blanco, V. Luaña, R. Pandey, L. Gerward, and J. Staun Olsen, *Phys. Rev. B* 58 (1998) 8949.
- [17] J. C. Jamieson, *Phys. Earth Planet. Inter.* 3 (1970) 201.
- [18] S. Desgreniers, *Phys. Rev. B* 58 (1998) 14102.
- [19] H. Karzel *et al.*, *Phys. Rev. B* 53 (1996) 11425.
- [20] D. J. Chadi, *Phys. Rev. Lett.* 72 (1994) 534.
- [21] T. Minami, H. Sato, H. Nanto, and S. Takata, *Jpn. J. Appl. Phys., Part 2* 24 (1985) 781.
- [22] A. F. Kohan, G. Ceder, D. Morgan, and C. G. Van de Walle, *Phys. Rev. B*
- [23] J. D. Albrecht, P. P. Ruden, S. Limpijumnong, W. R. L. Lambrecht, and K. F. Brennan, *J. Appl. Phys.* 86 (1991) 6864
- [24] C. G. Van de Walle, *Physica B* 308–310 (2001) 899.

- [25] S. F. J. Cox *et al.*, Phys. Rev. Lett. 86 (2001) 2601.
- [26] C. G. Van de Walle, Phys. Rev. Lett. 85 (2000) 1012.
- [27] H. Kato, M. Sano, K. Miyamoto, and T. Yao, J. Cryst. Growth 237–239 (2002) 538.
- [28] S. Y. Myong, S. J. Baik, C. H. Lee, W. Y. Cho, and K. S. Lim, Jpn. J. Appl. Phys., Part 2 36 (1997) 1078.
- [29] B. M. Ataev, A. M. Bagamadova, A. M. Djabrailov, V. V. Mamedov, and R. A. Rabadanov, Thin Solid Films 260 (1995) 19.
- [30] V. Assuncao, E. Fortunato, A. Marques, H. Aguas, I. Ferreira, M. E. V. Costa, and R. Martins, Thin Solid Films 427 (2003) 401.
- [31] H. J. Ko, Y. F. Chen, S. K. Hong, H. Wensch, T. Yao, and D. C. Look, Appl. Phys. Lett. 77 (2000) 3761.
- [32] Z. L. Wang, Mater. Today 7 (2004) 26.
- [33] Y. W. Heo, D. P. Norton, L. C. Tien, Y. Kwon, B. S. Kang, F. Ren, S. J. Pearton, and J. R. LaRoche, Mater. Sci. Eng., R. 47 (2004) 1.
- [34] X. Duan, Y. Huang, Y. Cui, J. Wang, and C. M. Lieber, Nature London 409, 66 2001.
- [35] M. H. Huang *et al.*, Science 292 (2001) 1897.
- [36] Z. L. Wang, X. Y. Kong, and J. M. Zuo, Phys. Rev. Lett. 91 (2003) 185502.
- [37] Z. Yang, X. Zong, Z. Ye, B. Zhao, Q. Wang, P. Wang, Biomaterials 31 (2010) 7534.
- [38] M. Willander, P. Klason, L.L. Yang, S.M. Al-Hilli, Q.X. Zhao, O. Nur, Phys. Stat.Solid. 5 (2008) 3076.
- [39] J.P. Liu, X.T. Huang, Y.Y. Li, X.X. Ji, Z.K. Li, X. He, F.L. Sun, J. Phys. Chem. C 111 (2007) 4990.
- [40] M. Ahmad, C. Pan, Z. Luo, J. Zhu, J. Phys. Chem. C 114 (2010) 9308.
- [41] H. Zhang, D. Yang, S. Li, X. Ma, Y. Ji, J. Xu, D. Que, Mater. Lett. 59 (2005) 1696.
- [42] S.M.U. Ali, T. Aijazi, K. Axelsson, O. Nur, M. Willander, Sensors-Basel 11 (2011) 8485.
- [43] R. Razali, A.K. Zak, W.H.A. Majid, M. Darroudi, Ceram. Int. 37 (2011) 3657.
- [44] G. Du, L. Zhang, Y. Feng, Y. Xu, Y. Sun, B. Ding, Q. Wang, Mater. Lett. 73 (2012) 86.
- [45] G. Amin, M.H. Asif, A. Zainelabdin, S. Zaman, O. Nur, M. Willander, J. Nanomater. 2011 (2011) Article ID 269692.
- [46] J. Zhao, L. Wu, J. Zhi, J. Mater. Chem. 18 (2008) 2459.
- [47] M.Q. Israr, J.R. Sadaf, M.H. Asif, O. Nur, M. Willander, B. Danielsson, Thin Solid Films 519

- (2010) 1106.
- [48] B.X. Gu, C.X. Xu, G.P. Zhu, S.Q. Liu, L.Y. Chen, X.S. Li, *J. Phys. Chem. B* 113 (2008) 377.
 - [49] A. Wei, X.W. Sun, J.X. Wang, Y. Lei, X.P. Cai, C.M. Li, Z.L. Dong, W. Huang, *Appl. Phys. Lett.* 89 (2006) 123902.
 - [50] L. Yu, F. Qu, X. Wu, *Appl. Surf. Sci.* 257 (2011) 7432.
 - [51] Z.H. Dai, K. Liu, Y.W. Tang, X.D. Yang, J.C. Bao, J. Shen, *J. Mater. Chem.* 18 (2008) 1919.
 - [52] J.P. Liu, X.T. Huang, Y.Y. Li, X.X. Ji, Z.K. Li, X. He, F.L. Sun, *J. Phys. Chem. C* 111 (2007) 4990.
 - [53] Z. Yang, Z. Ye, B. Zhao, X. Zong, P. Wang, *J. Sol-Gel Sci. Technol.* 54 (2010) 282.
 - [54] C. Xia, W. Ning, W. Long, G. Lin, *Sens. Actuat. B-Chem.* 147 (2010) 629.
 - [55] Y. Zhang, Y. Zhang, H. Wang, B. Yan, G. Shen, R. Yu, *J. Electroanal. Chem.* 627 (2009) 9
 - [56] X. Liu, Q. Hu, Q. Wu, W. Zhang, Z. Fang, Q. Xie, *Colloids Surf. B: Biointerfac.* 74 (2009) 154.
 - [57] G.-Q. Mo, J.-S. Ye, W.-D. Zhang, *Electrochim. Acta* 55 (2009) 511.
 - [58] H.J. Ko, Y.F. Chen, S.K. Hong, H. Wensch, T. Yao, D.C. Look, *Appl. Phys. Lett.* 77 (2000) 3761.
 - [59] T. Minami, *Thin Solid Films* 516 (2008) 5822.
 - [60] V. Bhosle, A. Tiwari, J. Narayan, *Appl. Phys. Lett.* 88 (2006) 032106.
 - [61] T. Minami, *Semicond. Sci. Technol.* 20 (2005) 35.
 - [62] B.K. Meyer, H. Alves, D.M. Hofmann, W. Kriegseis, D. Forster, F. Bertram, J. Christen, A. Hoffmann, M. Strasburg, M. Dworzak, U. Haboeck, A.V. Rodina, *Phys. Status Solidi* 241 (2004) 231.
 - [63] H. Agura, H. Suzuki, T. Matsushita, T. Aoki, M. Okuda, *Thin Solid Films* 445 (2003) 263.
 - [64] S.-M. Park, T. Ikegami, K. Ebihara, *Thin Solid Films* 513 (2006) 90.
 - [65] H. Ohta, M. Orita, M. Hirano, H. Tanji, H. Kawazoe, H. Hosono, *Appl. Phys. Lett.* 76 (2000) 2740.
 - [66] B.Z. Dong, G.J. Fang, J.F. Wang, W.J. Guan, X.Z. Zhao, *J. Appl. Phys.* 101 (2007) 033713.
 - [67] H. Kim, D.J. Kim, S.J. Park, H. Hwang, *J. Appl. Phys.* 89 (2001) 1506.
 - [68] J.O. Song, K.K. Kim, S.J. Park, T.Y. Seong, *Appl. Phys. Lett.* 83 (2003) 479.
 - [69] A.W. Ott, R.P.H. Chang, *Mater. Chem. Phys.* 58 (1999) 132.
 - [70] T. Minami, T. Yamamoto, T. Miyata, *Thin Solid Films* 366 (2000) 63.

- [71] H. Kim, C.M. Gilmore, J.S. Horwitz, A. Pique, H. Murata, G.P. Kushto, R. Schlaf, Z.H. Kafa, D.B. Chrisey, *Appl. Phys. Lett.* 76 (2000) 259.
- [72] S. Zhao, W. Liu, L. Yang, K. Zhao, H. Liu, N. Zhou, A. Wang, Y. Zhou, Q. Zhou, Y. Shi, J. *Phys. D: Appl. Phys.* 42 (2009) 185101.
- [73] K. Yoshino, S. Oyama, M. Kato, M. Oshima, M. Yoneta, T. Ikari, *J. Phys. Conf. Ser.* 100 (2008) 082019.
- [74] Q. Yu, W. Fu, C. Yu, H. Yang, R. Wei, Y. Sui, S. Liu, Z. Liu, M. Li, G. Wang, C. Shao, Y. Liu, G. Zou, *J. Phys. D: Appl. Phys.* 40 (2007) 5592.
- [75] S. Ilican, Y. Caglar, M. Caglar, F. Yakuphanoglu, *Appl. Surf. Sci.* 255 (2008) 2353.
- [76] Y. Yang, X.W. Sun, B.J. Chen, C.X. Xu, T.P. Chen, C.Q. Sun, B.K. Tay, Z. Sun, *Thin Solid Films* 510 (2006) 95.
- [77] A. Malik, Ana Seco, E. Fortunato, R. Martins, B. Shabashkevich, S. Piroszenko, *Semicond. Sci. Technol.* 13 (1998) 102.
- [78] K.-K. Kim, S.-d. Lee, H. Kim, J.-C. Park, S.-N. Lee, Y. Park, S.-J. Park, S.-W. Kim, *Appl. Phys. Lett.* 94 (2009) 071118.
- [79] J. Zhong, H. Chen, G. Saraf, Y. Lu, C.K. Choi, J.J. Song, D.M. Mackie, H. Shen, *Appl. Phys. Lett.* 90 (2007) 203515.
- [80] J.H. Lee, C.-Y. Chou, Z. Bi, C.-F. Tsai, H. Wang, *Nanotechnology* 20 (2009) 395704.
- [81] K. Ellmer, A. Klein, B. Rech (Eds.), *Springer Series in Materials Science*, vol. 104, Springer, Berlin, 2008.
- [82] M. Ogawa, *J. Chem. Soc. Chem. Commun.* 1149 (1996).
- [83] S. Tanaka, N. Nishiyama, Y. Egashira K. Ueyama *Chem. Comm.* 16 (2005) 2125
- [84] M. Ogawa, H. Ishikawa, T. Kikuchi, *J. Mater. Chem.* 8 (1998) 1783 (1998).

Chapter 2

Low temperature synthesis of ZnO nanorods using a seed layer of zinc acetate/sodium dodecyle sulfate nanocomposite

Aligned ZnO nanorods were synthesized by a simple hydrothermal method without calcination. A seed layer of zinc acetate (ZnAc_2)/sodium dodecyle sulfate (SDS) nanocomposite was used for a nucleation of ZnO nanorods. First, a ZnAc_2 / SDS composite was deposited on a Si substrate by spin-coating. And then, ZnO nanorods were grown under hydrothermal conditions at 90°C . ZnO crystals were grown in the direction of c -axis perpendicular to the surface of the Si substrate. However, nucleation did not occur on the substrate of a ZnAc_2 seed layer without SDS, indicating that the presence of the ZnAc_2 /SDS seed enhanced the nucleation of ZnO crystals. These results show that highly-dispersion of ZnAc_2 in the nanocomposite effectively assists a nucleation of ZnO crystals.

2.1 Introduction

Interaction between inorganic species and surfactant molecules has extensively studied in the field of mesostructured materials. The inorganic-organic nanopomposite with ordered mesostructures have been reported by many groups so far [1,2]. From a different point of view, one of the main advantages of these composites is highly dispersion of inorganic species in the composites. The objective in this study is to take advantage of the highly-dispersed inorganic species for the nucleation of the crystal of metal oxide.

Zinc oxide (ZnO) is a wide band gap (3.37 eV) semiconductor with a large binding energy (60 meV) and possesses unique optical and electronic properties. ZnO nanomaterials have been widely

studied for high-technology applications ranging from ultraviolet light-emitting diodes [3] to transducers [4], photodiodes [5], and gas sensors [6,7]. Various chemical, electrochemical, and physical deposition techniques have created structures of oriented ZnO nanorod arrays so far. For instance, metal–organic chemical vapor deposition [8], pulsed laser deposition [9], a vapor–liquid–solid epitaxial mechanism [10], epitaxial electrodeposition [11,12] and radiofrequency magnetron sputtering [5] have been performed to create highly oriented ZnO nanorods. However, these techniques require harsh reaction conditions, such as high pressures and high temperature, those limit its use in large-scale production.

Hydrothermal processes, on the other hand, permit a fabrication of large-scale aligned ZnO nanorods at relatively low cost and remarkably low temperatures without the need for metal catalysts [13,14]. In the previous reports on low-temperature synthesis, however, ZnO crystals layers were essential as a seed for the growth of ZnO nanorods. These processes contain calcination above 300 °C to form the ZnO crystal seed layers. Wu et al. demonstrated a one-step synthesis of oriented ZnO nanorods on an oxidized Zinc foil without seed layers [15]. Although they successively prepared highly-oriented ZnO nanorods on the surface of the zinc plate, it is still challenge to develop a low temperature synthesis of ZnO nanorods on various substrates other than the zinc-containing plate.

Oriented ZnO nanorods films on Zn-free substrates have not been hydrothermally synthesized at low temperature. In this study, we have first developed a simple synthesis method for ZnO nanorods arrays on a Si wafer without any calcination processes. This method enables the use of various substrates with low thermal stability. Here, a zinc acetate/surfactant composite was used as a seed layer without a pre-heating treatment. Several groups reported the crystal growth of ZnO in the presence of surfactants such as sodium dodecyle sulfate [16,17] and cetyltrimethylammonium bromide (CTAB) [18]. These surfactants play a role in the control of crystal morphology and size of ZnO particles. On the other hand, in this study, we mainly expected an enhancement of the nucleation of ZnO crystals using surfactants instead of the crystal growth. We have first used a zinc acetate/surfactant composite for the fabrication of oriented ZnO nanorods array films. The effect of the presence of surfactant in the seed layer on the formation of ZnO crystals is shown.

2.2 Experiment

2.2.1 ZnO Nanorods Synthesis by Hydrothermal Method

A solution for a seed layer was prepared from zinc acetate dihydrate ($\text{Zn}(\text{CH}_3\text{COO})_2 \cdot 2\text{H}_2\text{O}$: ZnAc_2), sodium dodecyl sulfate (SDS) and deionized water. The molar ratios of the solution were 2 ZnAc_2 : 0.07 SDS: 300 H_2O . The mixture was stirred for 1 h at room temperature. The solution was then spin-coated on a silicon substrate (4000 rpm, 1 min). The ZnAc_2 /SDS composite layer was dried at 90 °C for 8-24 h.

Solutions for a hydrothermal synthesis were prepared by dissolving zinc nitrate hexahydrate ($\text{Zn}(\text{NO}_3)_2 \cdot 6\text{H}_2\text{O}$) and 28% ammonium aqueous solution (NH_3aq) in distilled water (the molar ratios of the solution were 1 $\text{Zn}(\text{NO}_3)_2$: 2200 H_2O : x NH_3 , $x = 8$ (solution 1) and 17 (solution 2)). The ZnAc_2 /SDS composite layer on the Si substrate was immersed in the above solutions in a closed vessel. The vessel was then placed in an oven at 90 °C for 4 h. After hydrothermal synthesis, the samples were rinsed with deionized water and then dried at 90 °C.

2.2.2 Characterization

X-ray diffraction (XRD) patterns of the products were measured by X-ray diffractometer (Rigaku Mini-Flex) using monochromatized Cu $K\alpha$ with $\lambda = 1.5418$ Å. The morphology of the sample was analyzed by field emission scanning electron microscopy (FE-SEM: : Hitachi S-5000 L) at an acceleration voltage of 20 kV.

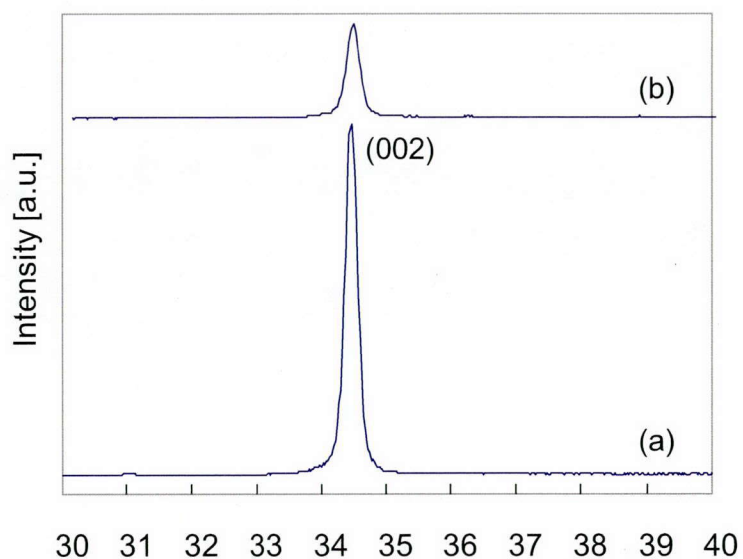


Fig. 2.1 XRD patterns of ZnO nanorods after hydrothermal synthesis using a solution with molar ratio of 1

$\text{Zn}(\text{NO}_3)_2 \cdot 6\text{H}_2\text{O}$: 33000 H_2O : x NH_3 . $x = (a)$ 17 and (b) 8.

2.3 Results and discussion

Fig. 1(a) shows the XRD pattern of the product after hydrothermal synthesis using solution (2) with the molar ratio of NH_3 , $x = 17$. In the XRD pattern, one strong reflection peak of (002) plane of ZnO crystal appeared. Peaks of (100) and (101) planes of ZnO crystal cannot be observed. These results indicate that the c-axis of the ZnO nanorods is perpendicular to the surface of the Si substrate.

FE-SEM images of the cross section and top view of the ZnO nanorods are shown in **Fig. 2(a)**. As expected from the XRD results, ZnO crystals are grown in the direction of c-axis perpendicular to the surface of the Si substrate. The diameter and length of ZnO nanorods are 50-100 nm and 2 μm , respectively. The top edge of the ZnO rods are sharp-pointed possibly because the diffusion resistance of ZnAc_2 increased as the rods extend, which decreased the crystal growth rate parallel to the film surface.

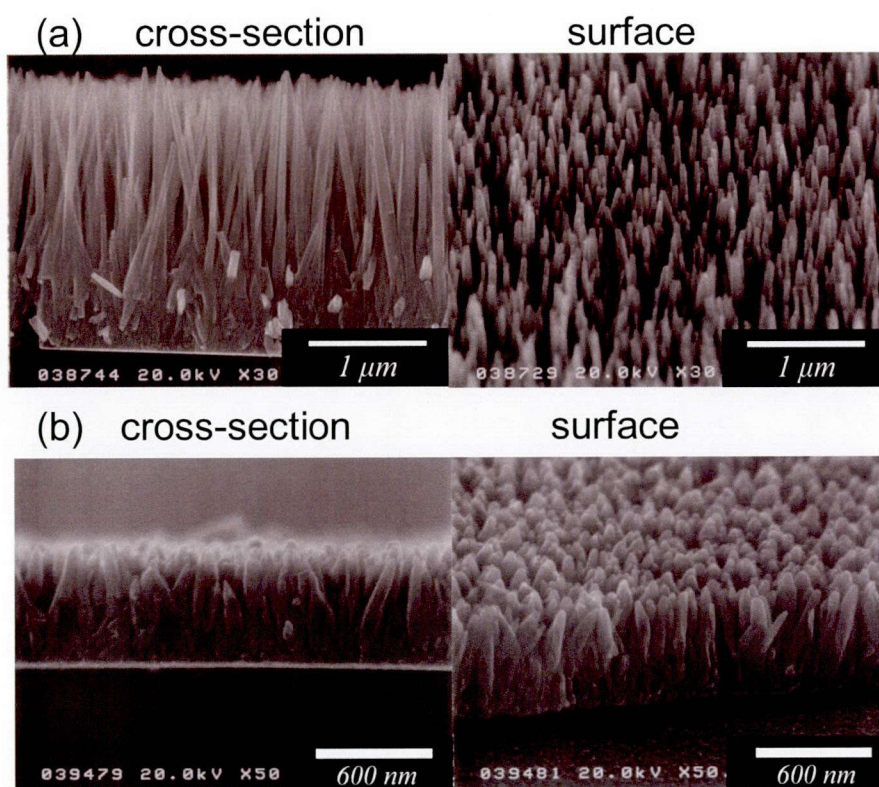


Fig. 2.2 FE-SEM images of ZnO nanorods using solutions with molar ratios of (a) 1 $\text{Zn}(\text{NO}_3)_2 \cdot 6\text{H}_2\text{O}$: 33000 H_2O : 17 NH_3 and (b) 1 $\text{Zn}(\text{NO}_3)_2 \cdot 6\text{H}_2\text{O}$: 33000 H_2O : 8 NH_3 .

Next, ZnO crystals were grown in the solution (1). Here, the molar ratio of NH_3 in hydrothermal solutions was reduced to half of the solution (2). **Fig. 1(b)** and **Fig. 2(b)** show the XRD pattern and

FE-SEM images of ZnO nanorods. The XRD pattern shows that ZnO nanorods were highly oriented in the direction of c-axis. The diameter of the ZnO nanorods was about 70 nm, which is comparable to the ZnO nanorods prepared using the solution (2). On

the other hand, the lengths of the ZnO nanorods were short (600 nm). With increasing the molar ratio of NH_3 , the lengths of the ZnO nanorods increased (data not shown). When the crystal growth rate is smaller, ZnAc_2 was sufficiently supplied into the film by diffusion, resulted in the formation of denser layer. The top edge of the ZnO nanorods is more rounded compared to the ZnO nanorods prepared from the solution (2).

For comparison, a Si substrate without a seed layer was treated with the same solutions under the hydrothermal conditions. However, any products were not formed on the substrate, indicating that the presence of the ZnAc_2/SDS seed enhanced the nucleation of ZnO crystals. In addition, when a ZnAc_2 solution without SDS was used for a seed layer, ZnO nanorods were not formed possibly because ZnAc_2 molecules aggregate together on the Si substrate due to a poor wettability of the solution on the Si surface. Furthermore, the growth rate and orientation of ZnO nanorods strongly depended on the concentration of SDS in the solutions. The ZnAc_2 molecules must interact with SDS to form a ZnAc_2/SDS composite. Thus, the ZnAc_2 molecules are uniformly dispersed on the Si substrate, which might affect the nucleation of ZnO nanorods.

From FE-SEM images of the ZnAc_2/SDS seed layer, a layer was not obviously observed because the layer was too thin. Considering the resolution of the FE-SEM images, the thickness of the ZnAc_2/SDS layer is less than 20 nm. In the XRD pattern of the ZnAc_2/SDS seed layer, no reflection peaks appeared because the layer was too thin. Thus, as a reference study, precursor solutions of

ZnAc_2/SDS were evaporated and then dried powder samples were measured by XRD. **Fig. 3** shows XRD patterns of ZnAc_2/SDA composite and SDS without ZnAc_2 . No reflection peaks for ZnO appeared indicating that the ZnAc_2/SDS seed layer was not crystallized during a drying at 90 °C. The XRD pattern of SDS powder shows that SDS molecules aggregate in a lamellar structure with a $d(001)$ spacing of 3.85 nm. New peaks for the

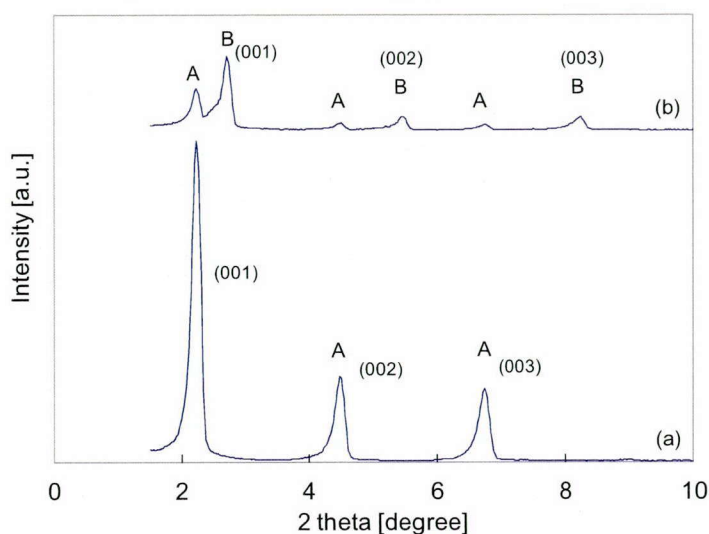


Fig. 2.3 XRD patterns of (a) SDS and (b) ZnAc_2/SDS composite. A: peaks for SDS, B: peaks for ZnAc_2/SDS composite.

ZnAc₂/SDS composite appeared. The composite shows a lamellar structure with a $d(001)$ spacing of 3.27 nm, which is smaller than that of SDS. In the ZnAc₂/SDS composite, Na⁺ ions in SDS must be partly exchanged by Zn²⁺ ion. Considering a decrease in the total number of the ions and smaller size of Zn²⁺ ion than Na⁺ ion, the reduction of the $d(001)$ spacing is a reasonable result. These results apparently suggest that ZnAc₂ molecules interact with SDS, and ZnAc₂ was highly dispersed in the composite.

We have reported on TEM observations of the ZnO crystal growth in the presence of ZnO seed crystals [19]. The formation process of amorphous ZnO nanoparticles on the surface of the seed crystals and their subsequent crystallization plays an important role in the induction of further crystal growth of ZnO nanorods. On the other hand, in this study, active amorphous ZnO species can be formed without using ZnO seed crystals. It seems like that the highly-dispersed ZnAc₂ molecules effectively assisted the nucleation of ZnO crystals under hydrothermal conditions even at low temperature.

2.4 Conclusions

Aligned ZnO nanorods were synthesized by a simple hydrothermal method without calcination. A seed layer of zinc acetate (ZnAc₂)/sodium dodecyl sulfate (SDS) nanocomposite was used for the nucleation of ZnO nanorods. The ZnAc₂/SDS layer was too thin to be observed by the FE-SEM, suggesting that the thickness is less than 20 nm. ZnO crystals were grown in the direction of c-axis perpendicular to the surface of the Si substrate. The diameter and length of ZnO nanorods are 50-100 nm and 0.6-2 μ m, respectively. On the other hand, any products were not formed on the surface of the ZnAc₂ seed layer without SDS, indicating that the presence of the ZnAc₂/SDS seeds enhanced the nucleation of ZnO crystals. These results show that highly-dispersion of ZnAc₂ in the nanocomposite plays a key role in the nucleation of ZnO crystals.

References

- [1] Kresge CT, Leonowicz ME, Roth WJ, Vartuli JC, Beck JS. *Nature* 1992;359:710–2.
- [2] Zhao D, Huo Q, Feng J, Chmelka BF, Stucky GD. *J. Am. Chem. Soc.* 1998;120:6024–36.
- [3] Ohta H, Kawamura KI, Orita M, Hirano M, Sarukura N, Hosono H. *Appl. Phys. Lett.* 2000; 77:475–7.
- [4] Arnold MS, Avouris P, Pan ZW, Wang ZL. *J. Phys. Chem. B* 2003; 107:659–63.
- [5] Lee JY, Choi YS, Kim JH, Park MO, Im S. *Thin Solid Films* 2002; 403:553–7.
- [6] Pan Z, Wang ZL, Comini E, Faglia G, Sberveglieri G. *Appl. Phys. Lett.*, 2002; 81:1869–71.
- [7] Xu J, Chen Y, Chen D, Shen J. *Sens. Actuators B.*, 2006; 113: 526–531.
- [8] Liang S, Sheng H, Liu Y, Hio Z, Lu Y, Shen H, *J. Cryst. Growth* 2001; 225:110–3.
- [9] Choi JH, Tabata H, Kawai T, *J. Cryst. Growth* 2001; 226:493–500.
- [10] Huang M, Wu Y, Feick H, Tran N, Weber E, Yang PD. *Adv. Mater.* 2001;13:113–6.
- [11] Saito N, Haneda H, Sekiguchi T, Ohashi N, Sakaguchi I, Koumoto K. *Adv. Mater.* 2002;14 :418–20.
- [12] Pauporté T, Lincot D, Viana B, Pellé F. *Applied Physics Letters*, 2006;89 :233112
- [13] Guo M, Diao P, Cai S. *J. Solid State Chem.* 2005;178:1864–73.
- [14] Liu C, Masuda Y, Wu Y, Takai O. *Thin Solid Films* 2006; 503:110–4.
- [15] Wu X, Bai H, Li C, Lu G, Shi G. *Chem. Commun.* 2006;1665–7.
- [16] Xie J, Li P, Li Y, Wang Y, Wei Y. *Mater. Chem. Phys.* 2009; 114: 943–7
- [17] Li P, Liu H, Xu F, Wei Y. *Mater. Chem. Phys.* 2008; 112:393–7.
- [18] Sum XM, Chen X, Deng ZX, Li YD. *Mater. Chem. Phys.* 2002; 78 :99–104.
- [19] Maruo T, Ueno N, Ichikawa S, Nishiyama N, Egashira Y, Ueyama K. *Matt. Lett.* 2009; 63: 2373–2376

Chapter 3

Low-temperature synthesis of ZnO nanorods using organic-inorganic composite as a seed layer

Well-aligned zinc oxide (ZnO) nanorods were synthesized using a low-temperature hydrothermal method employing a zinc/sodium dodecyl sulfate (Zn/SDS) composite as a seed layer. The results of X-ray diffraction measurements indicate that the Zn/SDS composite has a lamellar structure with an interlayer distance of 3.12 nm, which is shorter than that of the lamellar structure of SDS (3.82 nm) due to ion exchange between Zn and Na. The results of X-ray absorption fine structure analyses suggest that ZnO crystals start to grow after an induction period of 20–30 min. The length of nanorods and the aspect ratio of ZnO nanorods could be controlled by altering the molarity of ammonium and zinc nitrate in the growth solutions.

3.1 Introduction

Zinc oxide is an important semiconductor material, due to its direct wide band gap (3.37 eV) and high exciton binding energy (60 meV), and its application in optoelectronics, catalysts, sensors, and actuators. One-dimensional (1-D) ZnO nanostructures, such as nanobelts [1], nanotubes [2], nanohelices [3], nanorods, nanowires [4], and tower-like structures of ZnO nanocolumns [4-6] are attracting increasing research interest for application to sensing [7], optoelectronics [8], field emission [9], and piezoelectricity [10].

Numerous methods have in the past been employed to fabricate 1-D ZnO nanostructures, including thermal evaporation [1,3], chemical vapor deposition (CVD) [11-14], metal-organic chemical vapor deposition (MOCVD) [4-6,15], pulsed laser deposition (PLD) [16], radio frequency (RF) magnetron sputtering [17], template-based growth [18] and various solution-phase approaches [16,18-29]. The vertically-aligned single-crystal ZnO nanorods on R-plane-oriented Al₂O₃ (sapphire), GaN, ZnO, Ga-doped ZnO, etc., substrates were prepared by MOCVD [4-6],

PLD [16], and CVD [11,14]. The growth of aligned ZnO nanorods is considered to be a good candidate for light emitting and field emissions [4-6]. However, these gas-phase approaches generally require highly sophisticated equipment, expensive single-crystalline substrates for oriented growth, and elevated temperatures of 450–900 °C, and often face other limitations, such as poor sample uniformity and low product yield [30].

Hydrothermal processes, on the other hand, permit the fabrication of large-scale aligned ZnO nanorods at relatively low cost and remarkably low temperatures without the need for metal catalysts [31,32]. However, in this process ZnO crystals layers have proved essential as the seed for the growth of ZnO nanorods, combined with calcination at above 300 °C to form ZnO crystal seed layers. Wu *et al.* demonstrated a one-step synthesis of oriented ZnO nanorods on an oxidized zinc foil without seed layers [33]. Although they prepared highly oriented ZnO nanorods on the surface of zinc plate, the development of low-temperature synthesis of ZnO nanorods on various substrates other than zinc-containing plate remains a challenge.

We have developed a simple method of synthesizing ZnO nanorod arrays on a Si wafer without the need for a calcination process [34,35]. This method enables the use of various substrates with low thermal stability. In this study, we used a zinc acetate/surfactant composite as a seed layer without the need for pre-heating. Several groups have reported the crystal growth of ZnO in the presence of surfactants such as sodium dodecyl sulfate (SDS) [28,36,37] and bis (2-ethylhexyl) sulfosuccinate sodium (Aerosol OT) [38]. These surfactants play a role in the control of crystal morphology and size of ZnO particles. On the other hand, in this study, we mainly expected enhanced nucleation of ZnO crystals using surfactants, rather than crystal growth. We have used a seed layer of a zinc/sodium dodecyl sulfate (Zn/SDS) composite to fabricate oriented ZnO nanorod array films. As described above, various preparation methods for ZnO nanorods have been reported. This seeding technique, however, is so far the only known method of fabricating highly oriented ZnO nanorods films at low temperatures without using ZnO crystals as a seed or ZnO substrate, and provides opportunities for applications. However, this method cannot as yet control the morphology of ZnO nanorod films. It is important, to be able to control the morphology, to clarify the mechanisms of nucleation and crystal growth of ZnO nanorods. In this study, we studied the structure of the zinc/surfactant composite and its effect on the nucleation of the ZnO crystals. Following this, we were able to control the aspect ratios of the ZnO nanorods by changing the compositions of the growth solutions.

3.2 Experiment

3.2.1 Hydrothermal Synthesis of ZnO nanorods

In a typical procedure, a solution for a seed layer was prepared from zinc acetate dihydrate ($\text{Zn}(\text{CH}_3\text{COO})_2 \cdot 2\text{H}_2\text{O}$: ZnAc_2), SDS and deionized water. The molarities of the solution were 0.2 M ZnAc_2 and 0.014 M SDS. The mixture was stirred for 1 h at room temperature. The solution was then spin-coated on a silicon substrate (4000 rpm, 1 min). The Zn/SDS composite was finally dried at 90 °C for 8–24 h.

The seed layer was grown to ZnO nanorods via hydrothermal synthesis. Solutions for ZnO growth were prepared by dissolving zinc nitrate hexahydrate ($\text{Zn}(\text{NO}_3)_2 \cdot 6\text{H}_2\text{O}$) and 28% ammonium aqueous solution (NH_3 aq) in distilled water. The molarities of the growth solutions were 0.0125–0.0375 M $\text{Zn}(\text{NO}_3)_2$ and 0.1–0.6 M NH_3 . The Zn/SDS composite on the Si substrate was immersed in the above solutions in a closed vessel. The vessel was then placed in an oven at 90 °C for 0–8 h. After the growth reaction, the samples were rinsed with deionized water and then dried at 90 °C. ZnO nanorods were synthesized under the conditions listed in Table 1 and their morphology and orientation were then compared.

3.2.2 Characterization

X-ray diffraction (XRD) patterns of the 2×2 cm films were measured using an X-ray diffractometer (RigakuMini-Flex) employing monochromatized Cu K α with $\lambda = 1.5418 \text{ \AA}$ in the θ -2 θ Bragg-Brentano scan mode. The morphology of the sample was analyzed by field emission scanning electron microscopy (FE-SEM: Hitachi S5000 L) at an acceleration voltage of 20 kV. Zn L₃-edge X-ray absorption fine structure analyses (XAFS) were performed at the SR Center's BL-10 at Ritsumeikan University. Samples were loaded in the XAFS sample chamber under vacuum without exposure to air. XAFS spectra were obtained in the total electron yield mode.

Table 3.1 Molarities of the aqueous solutions for seed layer and growth of nanorods

sample	Solution for seed layer		Solution for growth solution	
	SDS [mol/L]	ZnAc ₂ [mol/L]	Zn(NO ₃) ₂ [mol/L]	NH ₃ [mol/L]
S1	0.014	0.2	0.025	0.4
S2	0	0.2	0.025	0.4
S3	0.014	0	0.025	0.4
S4	0.014	0.2	0.025	0.1
S5	0.014	0.2	0.025	0.2
S6	0.014	0.2	0.025	0.3
S7	0.014	0.2	0.025	0.6
S8	0.014	0.2	0.0125	0.4
S9	0.014	0.2	0.0375	0.4

3.3 Results and discussion

3.3.1 Effect of the solution composition for seed layer on the growth of ZnO nanorods

We have carried out a series of experiments with different solution compositions for both the seed layer and the growth of ZnO nanorods. The molarities of each component in the solutions are listed in **Table 3.1**. The FE-SEM images of the cross-section of the Zn/SDS seed layer and the film (S1) are shown in **Fig. 3.1**. The Zn/SDS composite film was a uniform 7–9 nm-thick layer. The ZnO nanorods grow in the direction of the *c*-axis, perpendicular to the surface of the Si substrate. The length of the nanorods was nearly 2 μm and their diameters were 50–100 nm.

Fig. 3.2(A) (a) shows an XRD pattern of the film (S1) using a Zn/SDS composite as a seed layer. We evaluated the degree of *c*-orientation of the ZnO crystals on the substrates using the peak intensity ratios of the (002) plane to the (101) plane of the ZnO crystal. The (002)/(101) peak intensity ratios are plotted in **Fig. 3.2(B)**. The (002)/(101) peak intensity ratio for the (S1) film is 80, much larger than that for ZnO powder (= 0.4), indicating that the ZnO nanorods were highly oriented and grew perpendicularly to the surface of the Si substrate. These results are consistent with the FE-SEM observations (**Fig. 3.1(b)**). As a reference study, seed solutions without SDS

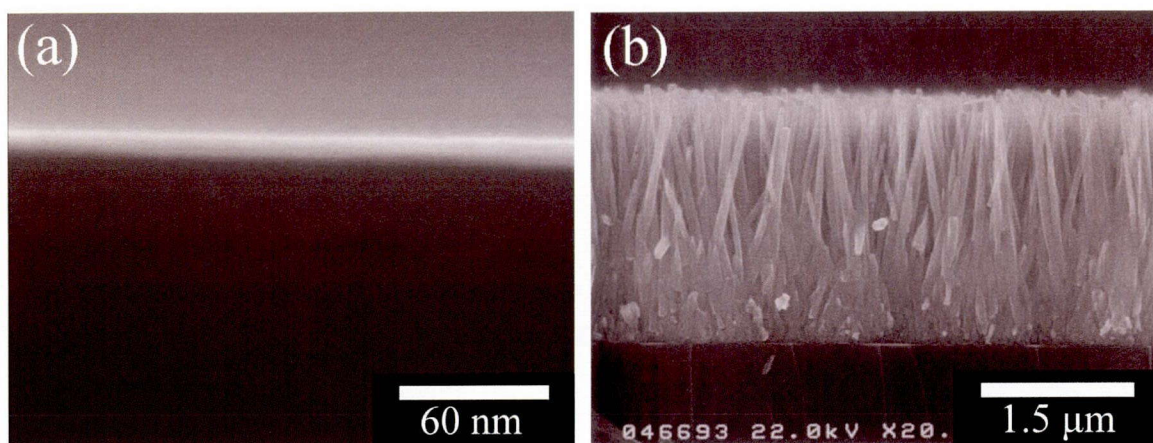


Fig. 3.1 FE-SEM images of (a) Zn/SDS composite layer and (b) the ZnO nanorods film.

Reaction time = 4 h.

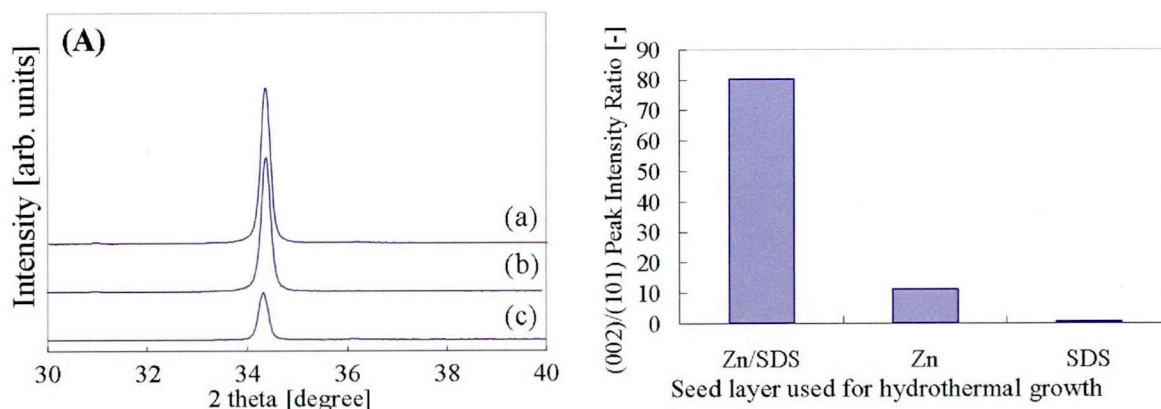


Fig. 3.2 (A) XRD patterns and (B) (002)/(101) peak intensity ratios of ZnO films prepared with 0.025 M $\text{Zn}(\text{NO}_3)_2$ and 0.4 M NH_3 growth solution from seed layers obtained using (a) 0.014 M SDS, (b) 0.2 M ZnAc_2 and (c) 0.014 M SDS and 0.2 M ZnAc_2 seed solution.

(S2) and without ZnAc_2 (S3) were used as seed layers. The XRD patterns of the films are shown in Fig. 3.2(A) and (B). The intensity ratios suggest that highly oriented ZnO nanorods do not grow on the Si support if SDS or ZnAc_2 are not present in the seed solution.

We have previously reported that the interlayer distances of the lamellar structure of the Zn/SDS composite are 3.41 and 3.12 nm, shorter than that of SDS [35]. Schematic illustrations of the possible structures of the SDS and Zn/SDS films are shown in **Fig. 3.3**. The results of the XRD patterns suggest that Zn ions are exchanged by Na ions in SDS to form a Zn/SDS composite with

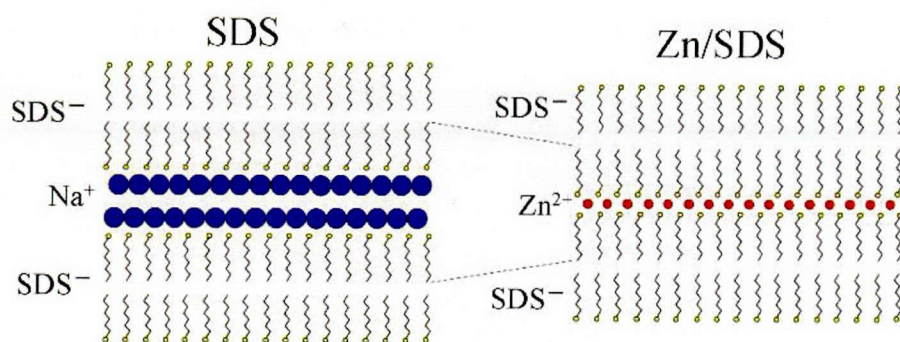


Fig. 3.3 Schematics of structures of SDS and Zn/SDS composite.

a lamellar symmetry. The ion size of Zn is smaller than that of Na, and two Na ions are replaced by one Zn ion, resulting in a shorter interlayer distance after the ion exchange. As a result, Zn ions were highly dispersed in the seed layer.

Fig. 3.4 shows the FE-SEM images of the (S1) films synthesized at different reaction times of 0.5 and 2 h. The time courses of the length and diameter of the nanorods are plotted in **Fig. 3.5**. The diameters of the tops of the nanorods are shown in this figure. The length of the nanorods increases in proportion to reaction time. However, the diameter of the nanorods did not increase with reaction time (Fig. 3.5). In the early stages of crystal growth, the nanorods were randomly oriented, as shown in Fig. 3.4(a). With a longer reaction time, however, ZnO nanorods grew selectively in the direction of the c-axis: crystal growth in other directions was inhibited due to steric crowding. The ZnO layer near the Si surface shown in Fig. 3.4(b) is likely to be

composed of randomly oriented and densely packed ZnO crystals.

Nucleation density on the Si surface at the early stage of growth is likely to be high to obtain highly c-oriented ZnO nanorods. The high dispersion of the Zn ions

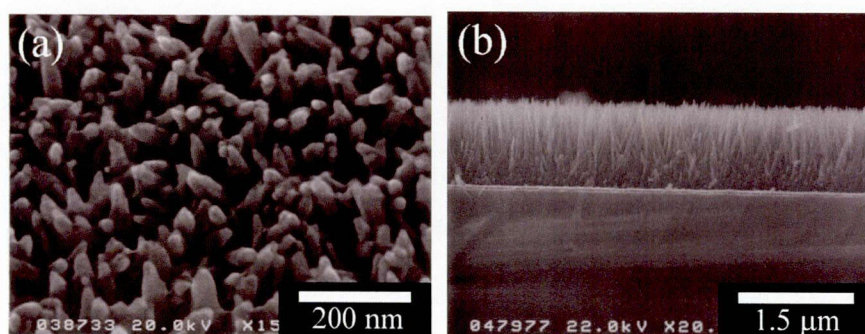


Fig. 3.4 FE-SEM images of ZnO nanorods with different growth reaction times. The molarities of growth solution are 0.025 M $\text{Zn}(\text{NO}_3)_2$ and 0.4 M NH_3 . Growth reaction time = (a) 0.5 h, (b) 2 h

in this study appears to play an important role in the nucleation of ZnO nanorods.

Fig. 3.5 suggests that nucleation starts after an induction period of 20–30 minutes. **Fig. 3.6** shows the XAFS patterns of the Zn/SDS seed layer and ZnO nanorods films synthesized at different times. The peaks for Zn ion in the Zn/SDS appeared at 1015 and 1038 eV. The intensity of the peaks decreased with reaction time and completely disappeared after 30 min. Instead, new peaks started to appear at 1017 and 1019 eV after 20 min, which are ascribed to ZnO crystal. The XAFS spectra did not change after 30 min. These results agree closely with other XRD and FE-SEM measurements.

3.3.2 Effect of solution composition on the growth of ZnO nanorods

In order to change the morphology of the films, we varied the molarities of NH_3 (S4-S7) in the growth solution. **Fig. 3.7** shows the XRD patterns and (002)/(101) peak intensity ratios of S1, S4, S5, S6 and S7. **Fig. 3.8** shows FE-SEM images of cross sections of the

S4 and S5 films. The lengths and diameters of the nanorods are plotted in **Fig. 3.9** as a function of the molarity of NH_3 . The (002)/(101) peak intensity ratio increased as the molarity of NH_3

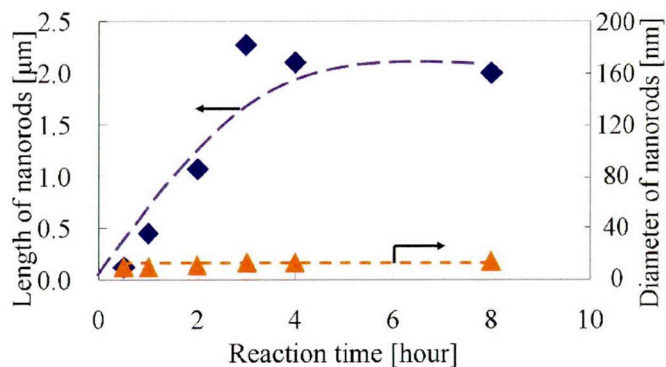


Fig. 3.5 The variation with growth reaction time in length and diameter of ZnO nanorods prepared with 0.025 M $\text{Zn}(\text{NO}_3)_2$ and 0.4 M NH_3 growth solution from seed layers obtained using 0.014 M SDS and 0.2 M ZnAc_2 seed solution.

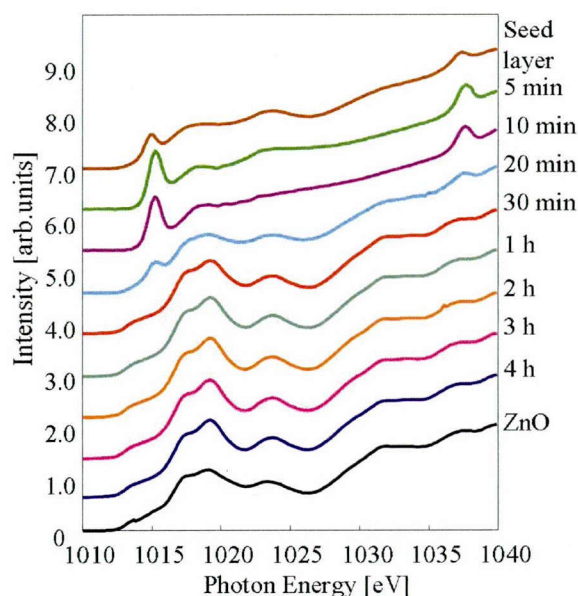


Fig. 3.6 XAFS spectra for the Zn/SDS seed and the ZnO nanorods films synthesized with 0.025 M $\text{Zn}(\text{NO}_3)_2$ and 0.4 M NH_3 growth solution from seed layers obtained using 0.014 M SDS and 0.2 M ZnAc_2 seed solution at different growth reaction times.

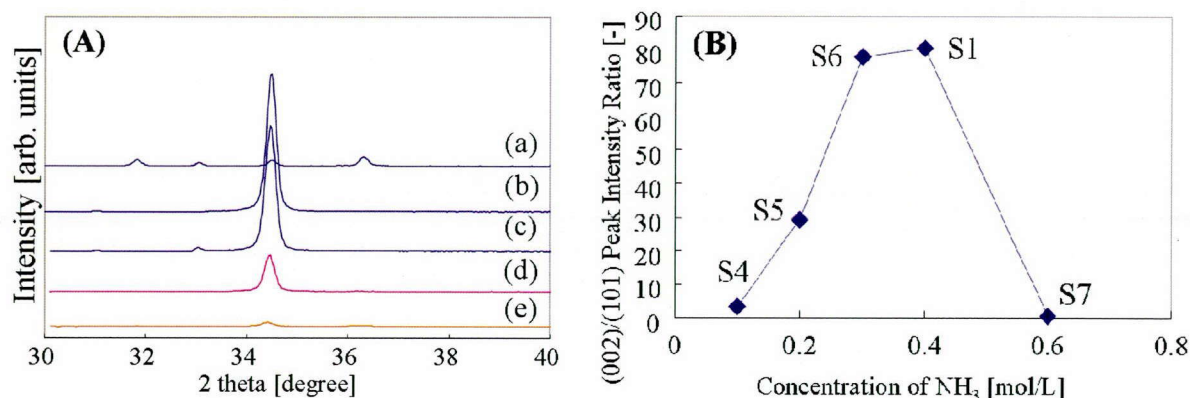
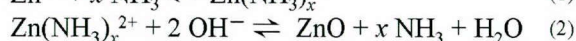
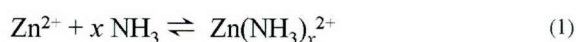


Fig. 3.7 (A) XRD patterns and (B) (002)/(101) peak intensity ratios of ZnO films prepared with 0.025 M Zn(NO₃)₂ and (a) 0.6 M (S7), (b) 0.4 M (S1), (c) 0.3 M (S6), (d) 0.2 M (S4) and (e) 0.1 M (S5) NH₃ growth solution (Reaction time = 4 h) from seed layers obtained using 0.014 M SDS and 0.2 M ZnAc₂ seed solution.

increased to 0.3. The length of the ZnO nanorods also increased on increasing the molarity of NH₃, but not the not the diameters, indicating that the aspect ratio diameters, indicating that the aspect ratio of nanorods can be changed by altering the molarity of NH₃. These results imply that the increased molarity of NH₃ did not affect the nucleation density at the Si surface but influenced the crystal growth.

However, when the molarity of NH₃ reached 0.3, the length did not increase any further, indicating that the crystal growth rate was not increased in this region. (Molarity of NH₃ = 0.3 - 0.4). Furthermore, nanorods could not be synthesized at an NH₃ molarity of 0.6. The concentration of NH₃ thus appears to be the key to the rate or growth of nanorods in the *c*-axis direction. Our results can be explained by the following mechanism for the formation of ZnO crystal [31,39,40].



Possible mechanisms for nucleation and crystal growth are proposed as follows. First, the Zn ions in the Zn/SDS seed layer react with NH₃ to form ammine complexes of zinc (Eq. (1)). Nucleation of ZnO nanocrystals then occurs in the seed layer as a result of this reaction (2). The ammine complex of zinc is also formed in the solution thorough the reaction of Zn ions(Zn(NO₃)₂) and NH₃. The ammine complex diffuses and is adsorbed onto the crystal surface.

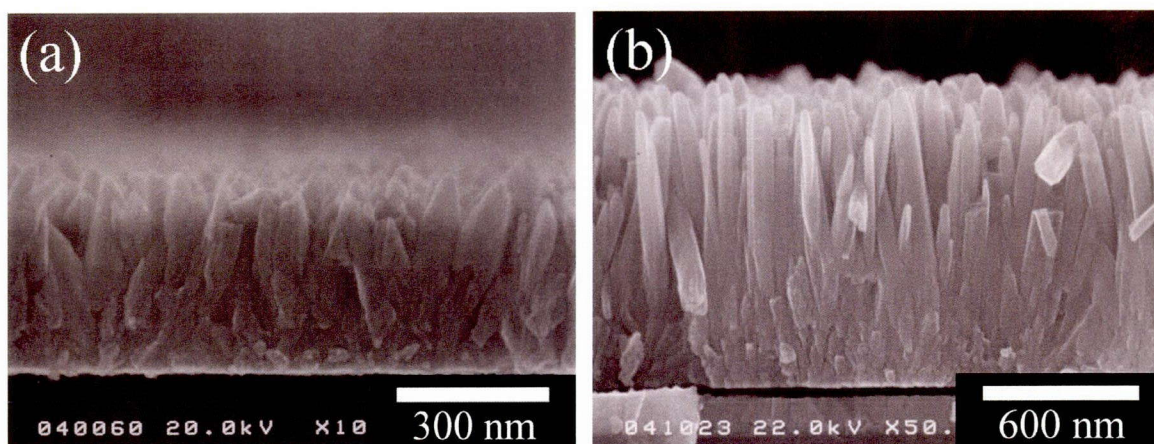


Fig. 3.8 FE-SEM images of cross-sections of zinc oxide nanorods films whose molarities of growth solution are 0.025 M $\text{Zn}(\text{NO}_3)_2$ (a) 0.1 M (S4) and (b) 0.2 M (S5) NH_3 .

The crystal growth proceeds by reaction (2). These reactions suggest that a high NH_3 concentration favors the presence of the $\text{Zn}(\text{NH}_3)_4^{2+}$ species, which decreases the growth rate and the amount of ZnO crystal. This shows good agreement with another report that does not use a seed layer [27].

Both reactions (1) and (2) are equilibrium reactions. On increasing the concentration of NH_3 , the concentration of ammine complex increases, resulting in an increase in the rate of the second reaction. However, at very high concentrations of NH_3 , the reverse reaction of the second reaction (dissolution of ZnO crystal) predominates. The results shown in Fig. 3.9 are in good agreement with the reaction mechanism described above.

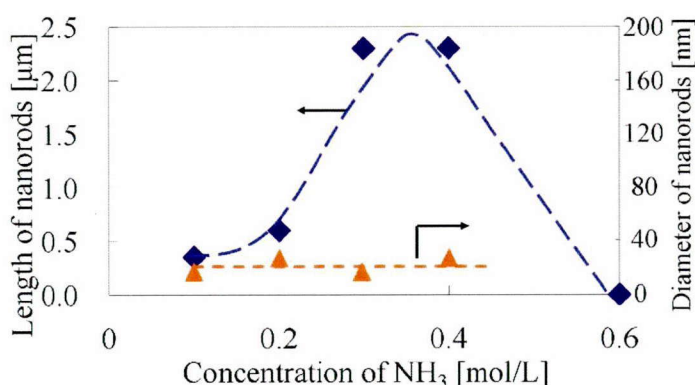


Fig. 3.9 Length and diameter of the ZnO nanorods as a function of the molarity of NH_3 in the growth solution. (Growth reaction time = 4 h.) ZnO did not grow when the molarities of NH_3 were < 0.1 M and > 0.4 M.

The molarity of $\text{Zn}(\text{NO}_3)_2$ in the growth solution was also changed (S8-S10). The XRD patterns and the (002)/(101)

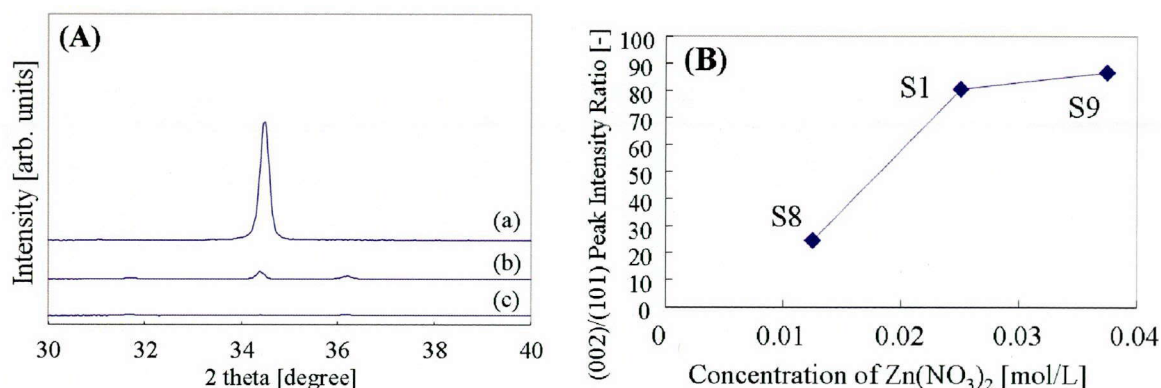


Fig. 3.10 (A) XRD patterns and (B) (002)/(101) peak intensity ratios of ZnO films prepared with (a) 0.025 M (S1), (b) 0.0125 M (S8) and (c) 0.0375 M (S9) Zn(NO₃)₂ and 0.4 M NH₃ growth solution from seed layers obtained using 0.014 M SDS and 0.2 M ZnAc₂ seed solution.

peak intensity ratios of S8 and S9 as well as S1 are shown in **Fig. 3.10**. The lengths and diameters of the ZnO nanorods were determined from FE-SEM images and are plotted in **Fig. 3.11**. The length of the nanorods is roughly proportional to the molarity of Zn(NO₃)₂, suggesting that the concentration of Zn ions is also an effective factor for controlling the growth rate of the ZnO nanorods. The diameter of nanorods also slightly decreases with increasing Zn(NO₃)₂ molarity, since the relative growth rate in the direction of the c axis to a/b axis is increased as a result. The results suggest that an increased concentration of Zn ion enhances the reaction rate of Eq. (1), resulting in an increase in the concentration of the ammine complex.

Thus, the crystal growth in the c-direction as well as its aspect ratio can be controlled by changing the concentrations of Zn ion and NH₃ in the solution. The highly oriented crystal growth in the c-direction resulted from the high nucleation density in the first 20 minutes.

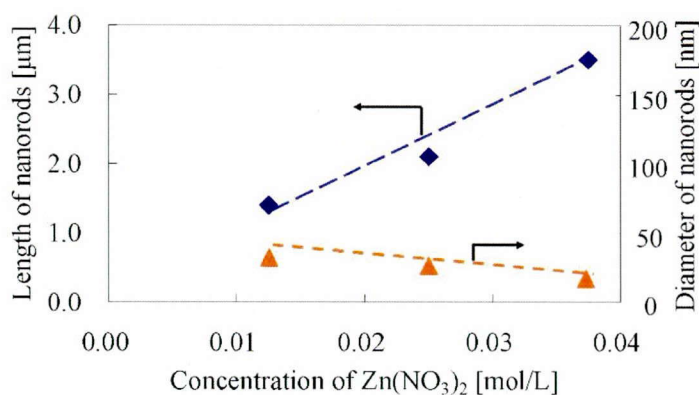


Fig. 3.11 Length and diameter of the ZnO nanorods as a function of the molarity of Zn(NO₃)₂ in the growth solution. (Reaction time = 4 h.)

3.3.3 Effect of handling of solution on the growth of ZnO nanorods

In the previous study, the ZnO crystal was grown under static conditions. Here, a growth solution was stirred or continuously supplied to control the morphology of the ZnO nanorods. **Fig. 3.12** shows the relationship between the length of the nanorods and the stirring rate. Under the static condition, the length of nanorods was 1.5 micrometer after the synthesis period of 4h. The nanorods prepared under stirring condition were longer than that those under static condition. The high growth rate of nanorods in the direction of lengthwise indicates that a fluid film on the surface of nanorods was thinned by stirring, which increases the feed rate of zinc ions to the top of nanorods.

The reaction rate for the crystal growth seems to be governed by diffusion limitation. However, the length of the nanorods shortened with increasing the stirring rate. The downward flow which

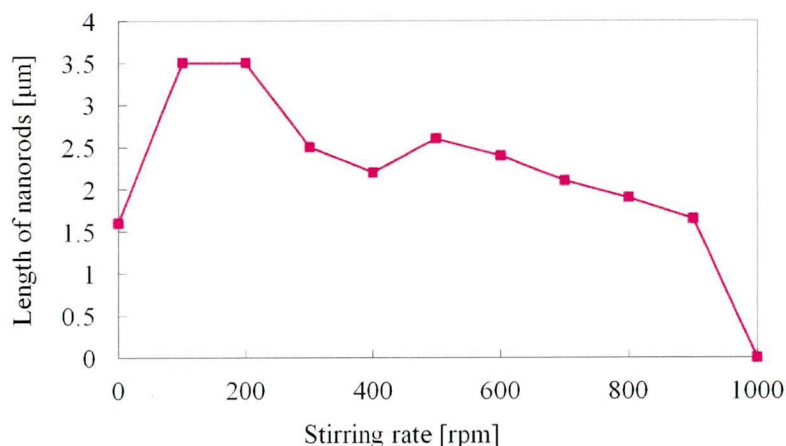


Fig. 3.12 Length of the ZnO nanorods as a function of the stirring rate of the growth solution. (Growth reaction time = 4 h.) The molarities of growth solution are 0.025 M $\text{Zn}(\text{NO}_3)_2$ and 0.4 M NH_3 .

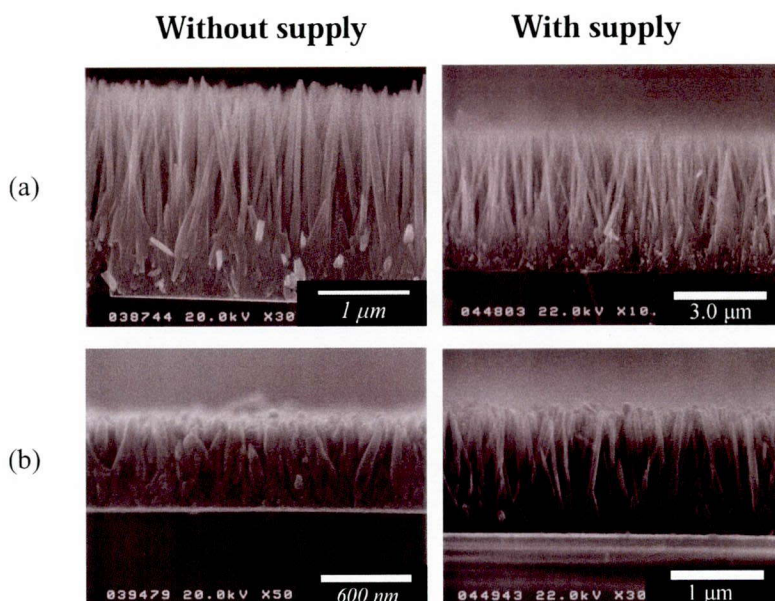


Fig. 3.13. FE-SEM images of cross-sections of zinc oxide nanorods films whose molarities of growth solution are 0.025 M $\text{Zn}(\text{NO}_3)_2$ (a) 0.4 M (S1) and (b) 0.2 M (S5) NH_3 .

leaves from the substrate surface becomes faster with increasing of stirring rate, which inhibited the supply of zinc ions to the nanorods. Consequently, the morphology (aspect ratio) could be controlled by changing stirring conditions.

Furthermore, the nanorods were inclined when the stirring rate was more than 700 rpm. At last, nanorods and seed layer were peeled off from the substrate when the stirring rate was over 1000 rpm.

Next, the nanorods were grown under a continuous supply of a growth solution. **Fig. 3.13** shows the FE-SEM images of ZnO nanorods which was synthesized with and without a supply of the growth solution. The nanorods prepared with the continuous supply were twice longer than those without the supply even though the same solution was used for both the cases.

Fig. 3.14 shows the time course of the concentration of zinc, pH, and temperature of the growth solution and length of synthesized nanorods. The concentration of zinc, pH, and temperature of the solution did not change after the crystal growth started. The high growth rate under a continuous supply indicates that the thermal history of the solution is related to the rate of crystal growth. Namely, the rate of reversible reaction (eq. (2)) reaches quasi-equilibrium state after a certain period of heating time.

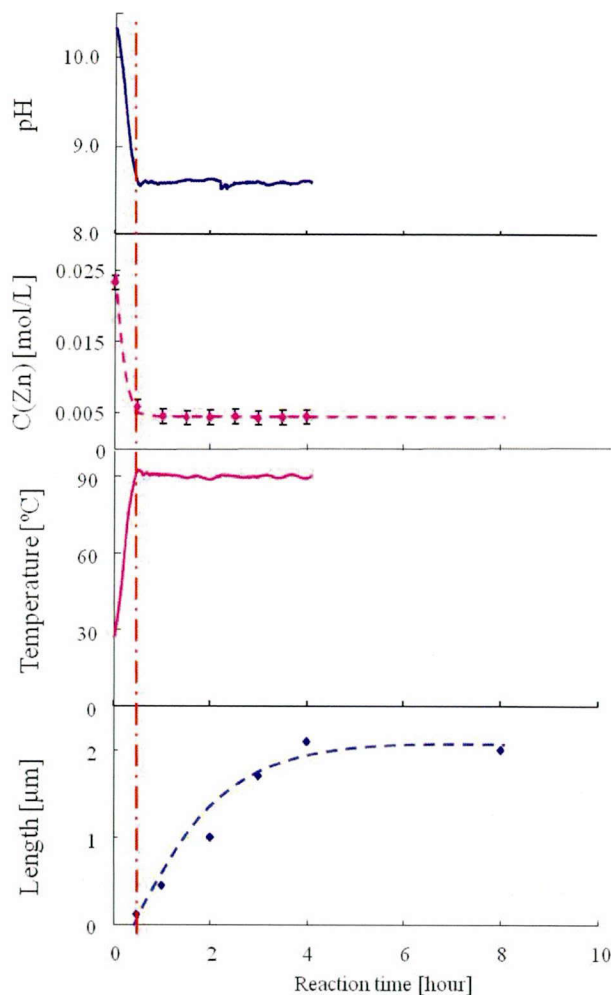


Fig. 3.14 Changes of the pH, concentration of Zn, temperature of growth solution and length of nanorods over the reaction time (The solution was prepared at room temperature. After that the vessel containing the solution is placed at an oven at 90°C)

3.4 Conclusions

Well-aligned ZnO nanorods were synthesized using the Zn/SDS composite seed layer. The Zn/SDS composite has a lamellar structure with an interlayer distance of 3.12 nm. High dispersion of the Zn ions in the composite layer appears to play an important role in the high nucleation density of ZnO nanorods, which contributes to the highly oriented crystal growth in the *c*-direction. The crystal growth in the *c*-direction as well as the aspect ratio could be controlled in the same way as when not using a seed layer, namely, by changing the concentration of Zn ions and NH₃ in the solution.

References

- [1] O. Lupan, L. Chow, G. Chai, L. Chernyak, O. Lopatiuk-Tirpak, H. Heinrich, *Phys. Status Solidi* 205 (2008) 2673.
- [2] O. Lupan, G. Chai, L. Chow, Technical Proceedings of the 2008 NSTI Nanotechnology Conference and Trade Show, NSTI-Nanotech, Nanotechnology June 1-5, (2008) Boston, Massachusetts, Vol. 3, pp 5-8.
- [3] S. D. Lee, Y. S. Kim, M. S. Yi, J. Y. Choi, S. W. Kim, *J. Phys. Chem. C* 113 (2009) 8954.
- [4] O. Lupan, T. Pauporté, B. Viana, *Adv. Mat.* 22 (2010) 3298.
- [5] X. Fang, J. Li, D. Zhao, D. Shen, B. Li, X. Wang, *J. Phys. Chem. C* 113 (2009) 21208.
- [6] C. H. Chen, S. J. Chang, S. P. Chang, M. J. Li, I. C. Chen, T. J. Hsueh, C. L. Hsu, *Appl. Phys. Lett.* 95 (2009) 223101.
- [7] Y. Ohno, T. Shirahama, S. Takeda, A. Ishizumi, Y. Kanemitsu, *Appl. Phys. Lett.* 87 (2005) 043106.
- [8] O. Lupan, G. Chai, L. Chow, *Microelectron. J.* 38 (2007) 1211.
- [9] O. Lupan, V. V. Ursaki, G. Chai, L. Chow, G. A. Emelchenko, I. M. Tiginyanu, A. N. Gruzintsev, A. N. Redkin, *Sens. Actuators B* 144 (2010) 56.
- [10] S. B. Zhang, S. H. Wei, A. Zunger, *Phys. Rev. B* 63 (2001) 075205.
- [11] H. J. Egelhaaf, D. J. Oelkrug, *Cryst. Growth* 161 (1996) 190.
- [12] A. Gulino, I. Fragala, *Chem. Mater.* 14 (2002) 116.
- [13] K. K. Kim, H. S. Kim, D. K. Hwang, J. H. Lim, S. Park, *J. Appl. Phys. Lett.* 83 (2003) 63.
- [14] K. Y. Gao, T. Seyller, L. Ley, F. Ciobanu, G. Pensl, A. Tadich, J. D. Riley, R. G. C. Leckey, *Appl. Phys. Lett.* 83 (2003) 1830.
- [15] D. C. Look, G. M. Renlund, R. H. Burgener, J. R. Sizelove, *Appl. Phys. Lett.* 85 (2004) 5269.
- [16] Y. J. Zeng, Z. Z. Ye, W. Z. Xu, D. Y. Li, J. G. Lu, L. P. Zhu, B. H. Zhao, *Appl. Phys. Lett.* 88 (2006) 062107.
- [17] F. T. Chung, A. J. Zapien, S. T. Lee, *J. Phys. Chem. C* 112 (2008) 820.
- [18] S. Limpijumnong, S. B. Zhang, S. H. Wei, C. H. Park, *Phys. Rev. Lett.* 92 (2004) 155504.
- [19] X. Pan, Z. Ye, J. Li, X. Gu, Y. Zeng, H. He, L. Zhu, Y. Che, *Appl. Surf. Sci.* 253 (2007) 5067.
- [20] F. X. Xiu, Z. Yang, L. J. Mandalapu, D. T. Zhao, J. L. Liu, W. P. Beyermann, *Appl. Phys. Lett.* 87 (2005) 152101.

- [21] F. X. Xiu, Z. Yang, L. J. Mandalapu, D. T. Zhao, J. L. Liu, Appl. Phys. Lett. 87 (2005) 252102.
- [22] H. S. Kang, B. D. Ahn, J. H. Kim, G. H. Kim, S. H. Lim, H. W. Chang, S. Y. Lee, Appl. Phys. Lett. 88 (2006) 202108.
- [23] I. S. Kim, E. K. Jeong, D. Y. Kim, M. Kumar, S. Y. Choi, Appl. Surf. Sci. 255 (2009) 4011.
- [24] Y. F. Yan, S. H. Wei, Phys. Status Solidi B 245 (2008) 641.
- [25] S. Cho, S. Kim, H. J. Kim, B. R. Lee, K. H. Lee, Langmuir 25 (2009) 10223-10229.
- [26] K. S. Jha, C. P. Liu, Z. H. Chen, K. J. Chen, I. Bello, J. A. Zapien, W. Zhang, S. T. Lee, J. Phys. Chem. C 114 (2010) 7999.
- [27] M. Ortega-Lo'pez, A. Avila-Garci'a, M.L. Albor-Aguileraa, V.M. Sa'nchez Resendiz, Mater. Res. Bull. 38 (2003) 1241.
- [28] J. Yahiro, T. Kawano, H. Imai, J. Colloid Interface Sci. 310 (2007) 302.
- [29] M. N.R. Ashfold, R. P. Doherty, N. G. Ndifor-Angwafor, D. J. Riley, Y. Sun, Thin Solid Films 515 (2007) 8679
- [30] V. Strikant, D. R. Clark, J. Mater. Res. 12 (1997) 1425.
- [31] M. Guo, P. Diao, S. Cai, J Solid State Chem. 178 (2005) 1864.
- [32] C. Liu, Y. Masuda, Y. Wu, O. Takai, Thin Solid Films 503 (2006) 110.
- [33] X. Wu, H. Bai, C. Li, G. Lu, G. Shi, Chem. Commun. (2006) 1665.
- [34] T. Maruo, N. Ueno, S. Ichikawa, N. Nishiyama, Y. Egashira, K. Ueyama, Mater Lett 63 (2009) 2373.
- [35] N. Ueno, T. Maruo, N. Nishiyama, Y. Egashira, K. Ueyama, Mater. Lett. 64 (2010) 513.
- [36] J. Xie, P. Li, Y. Li, Y. Wang, Y. Wei, Mater. Chem. Phys. 114 (2009) 943.
- [37] P. Li, H. Liu, F. Xu, Y. Wei, Mater Chem Phys 112 (2008) 393.
- [38] X. M. Sum, X. Chen, Z. X. Deng, Y. D. Li, Mater Chem Phys 78 (2002) 99.
- [39] W. Zhuo, Q. Xue-feng, Y. Jie, Z. Zi-kang, Langmuir 20 (2004) 3441.
- [40] S. Cho, S. Kim, H. N. Kim, J. U. Lee, S. H. Jung, E. Oh, K. H. Lee, J. Phys. Chem. C 112 (2008) 17760.

Chapter 4

Low-temperature hydrothermal synthesis of ZnO nanosheet using organic/inorganic composite as seed layer

Zinc oxide (ZnO) and Al-doped zinc oxide (AZO) nanorods were hydrothermally synthesized at low temperature using an organic/inorganic composite seed layer. The ZnO and AZO films had a sheet-like structure when ethanol was used as a solvent. The thickness of ZnO nanosheets can be controlled from 450 nm to 5.0 μm by altering the concentration of a zinc source in a growth solution. The ZnO and AZO nanosheets have a flat surface and high transparency (more than 90%) of visible light.

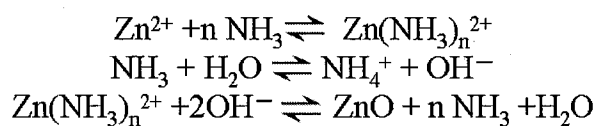
4.1 Introduction

Zinc oxide (ZnO) is a wide band gap (3.37 eV) semiconductor with a large binding energy (60 meV) and possesses unique optical and electronic properties. ZnO crystallizes in the hexagonal structure with zinc atoms in the tetrahedral sites, and lattice parameters $a=3.25 \text{ \AA}$ and $c=5.20 \text{ \AA}$. So far, ZnO nanomaterials have been widely studied for high-technology applications ranging from ultraviolet light-emitting diodes[1] to transducers[2], photodiodes[3], and gas sensors[4].

ZnO-based thin films exhibit high transparency and low resistivity and this material is suitable for the fabrication of solar cells[5] and flat panel display electrodes[6]. They also find applications as surface acoustic devices[7], optical waveguides[8], gas sensors[9] and micro-machined actuators[10]. ZnO thin films have been prepared by physical deposition methods such as laser deposition[11], different sputtering methods[5,7,12,13], atomic layer deposition and chemical deposition methods such as chemical vapor deposition[10], spray pyrolysis[14], chemical bath deposition[15] and the sol gel process[16].

Recently, we have reported that *c*-axisly oriented ZnO nanorods can be synthesized by using an organic/ inorganic composite as a seed layer[17]. ZnO nanorods were grown at very low

temperature without any metal catalysts or seed crystals. Synthesis reactions of ZnO are shown in the following equations.



First, zinc ammine complexes are formed by the reaction of ammonia and zinc ions in the growth solution or on the seed layer. Then, ZnO is formed by the reaction of the complexes with hydroxide ions. But, so far, it has been reported that nucleation occurs only in the presence of ZnO seed crystals for hydrothermal synthesis. On the other hand, we have found that nucleation occurs even at low temperature using Zn ions which are highly dispersed in a sodium dodecyl sulfate (SDS) seed layer[17]. The objective of the present study is to modify this technique to control the morphology of the ZnO films.

4.2 Experiment

4.2.1 Synthesis of ZnO nanosheet

The crystal growth was conducted in different solvents (water and ethanol) at 90°C. First, the composite layer of zinc ions and SDS was prepared by spin-coating the solution containing zinc acetate dihydrate (ZnAc_2). The molar ratio of the solution was 2 ZnAc_2 : 0.07 SDS : 300 H_2O . The mixture was stirred for 1 h at room temperature. The mixture was then, spin-coated on a silicon substrate (4000 rpm, 1 min). The seed layer was dried at 90°C for 8-24 h. Hydrothermal solutions were prepared by dissolving zinc nitrate ($\text{Zn}(\text{NO}_3)_2$) and ammonium aqueous solution (NH_3aq) in mixed solvents of distilled water and alcohol. After dried, the substrate with the seed layer was placed in an autoclave containing the growth solution. The autoclave was then put into oven at 90°C for 4 h. The molar ratios of the growth solutions are listed in **Table 4.1**. The sample ZnO-W1 was prepared using water as solvent. On the other hand, The samples, ZnO-M1, -E1, -E2, -E3, and -P1 were prepared using water/methanol (-M1), ethanol (-E1, -E2, -E3) or 1-propanol (-P1) mixed solvents. For the synthesis of Al-doped ZnO (AZO), $\text{Al}(\text{NO}_3)_3$ was added to growth solutions (sample AZO-E1).

Table 4.1 Molar ratio of growth solution

sample	Zn(NO ₃) ₂	NH ₃	H ₂ O	MeOH	EtOH	PrOH	Al(NO ₃) ₃
ZnO-W1	1	17	2200	0	0	0	0
ZnO-M1	1	17	550	740	0	0	0
ZnO-P1	1	17	550	0	0	400	0
ZnO-E1	1	17	550	0	520	0	0
ZnO-E2	2	17	550	0	520	0	0
ZnO-E3	3	17	550	0	520	0	0
AZO-E1	1	17	550	0	520	0	0.01

4.2.2 Characterizations

X-ray diffraction (XRD) patterns of the 2×2 cm films were measured using an X-ray diffractometer (RigakuMini-Flex) employing monochromatized Cu K α with $\lambda = 1.5418 \text{ \AA}$ in the θ -2 θ Bragg-Brentano scan mode. The morphology of the sample was analyzed by field emission scanning electron microscopy (FE-SEM: Hitachi S5000 L) at an acceleration voltage of 20 kV. The transparencies of the 1×2 cm ZnO films were investigated by ultra violet-visible absorbance measurement (UV-vis: Jasco V-570 UV/VIS/NIR spectrophotometer) in transmittance mode. The resistivity was analyzed by four probe method (MITSUBISHI CHEMICAL ANALYTECH Loresta-AX)

4.3 Results and Discussion

Fig. 4.1 shows the FE-SEM images of the ZnO-W1, M1, E1, and P1 films. Morphology of the ZnO films depends on the type of solvents. The lengths of the ZnO-W1, M1, E1 and P1 rods were 2 μm , 2 μm , 0.6 μm and 7 μm , respectively. The diameters were 20-80 nm, 50-80 nm, 100-130 nm and 1-1.6 μm , respectively. The difference of the diameters and aspect ratio of ZnO nanorods

was remarkable. The diameter of the rods was large when water and methanol were used as a solvent. This result indicates that nucleation density of ZnO crystals was high in these solvents. On the other hand, in the bulky alcohols (ethanol and propanol), nucleation density seems to be low, resulting the large diameters.

Figs. 4.2 and 4.3 show FE-SEM images and XRD

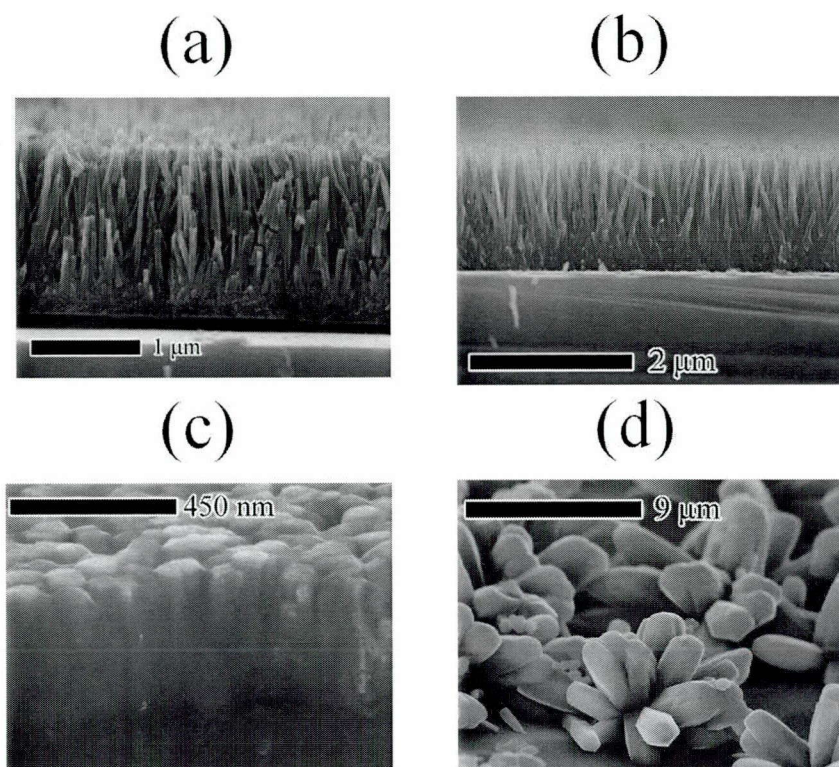


Fig. 4.1 FE-SEM images of ZnO films (a) ZnO-W1, (b) ZnO-M1, (c) ZnO-E1, and (d) ZnO-P1

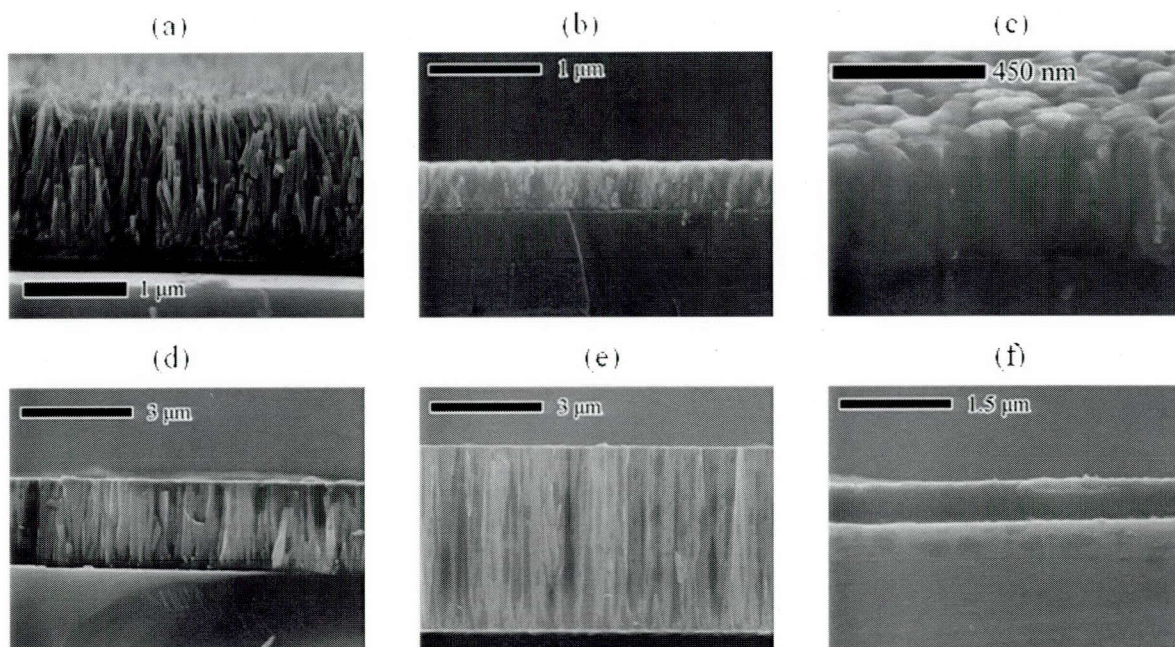


Fig. 4.2 FE-SEM images of ZnO and AZO films (a) ZnO-W1, (b) (c) ZnO-E1, (d) ZnO-E2, (e) ZnO-E3 and (f) AZO-E1

patterns of ZnO-W1, E1, E2, E3 and AZO-E1 samples. The ZnO-W1 film has a rod-like structure with interstices between the ZnO rods which are *c*-axisly oriented. The ZnO-E1, E2 and E3 films also have a *c*-axisly oriented structure. But, unlike the ZnO-W1 film, they show a sheet-like structure without interstices. Their surfaces are very flat. The thickness of ZnO-E1 nanosheet

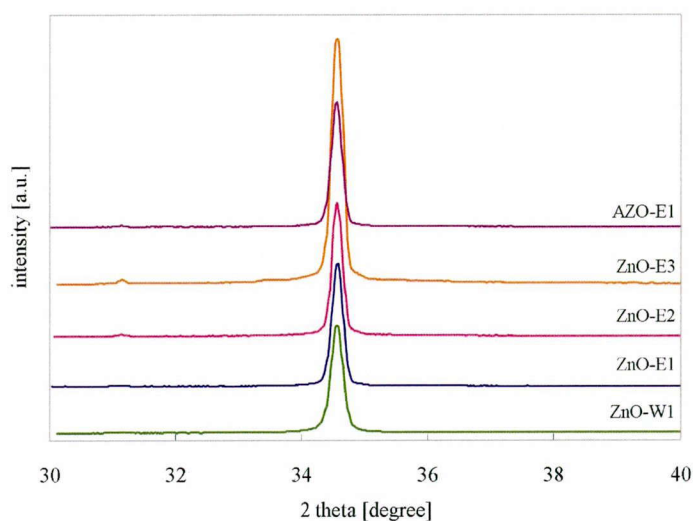


Fig. 4.3 XRD patterns of the ZnO-W1, E1, E2, E3 and AZO-E1 films

was 450 nm which is nearly one-quarter of the length of ZnO-W1 nanorods even though the reaction time and temperature are the same.

This fact indicates that the growth rate of ZnO was decreased by adding ethanol in the solvent. Furthermore, a homogeneous nucleation of ZnO did not occur in the growth solution when ethanol was included in the solvent. The Zn ions dispersed in the SDS film apparently play an important role in the heterogeneous nucleation of ZnO. In the growth solution, zinc ammine complex ion and hydrated zinc ion and ZnO are held in equilibrium as shown in **Fig. 4.4**. Zinc ammine complex has low polarity because of its tetrahedral structure. It seems like that dissolved zinc ammine complex was stable in the ethanol-containing solution with a less polarity than water, which resulted in less reactivity to form ZnO. The thickness of the ZnO nanosheets were increased to 2.5 (ZnO-E2) and 5.0 (ZnO-E3) μm when the concentration of $\text{Zn}(\text{NO}_3)_2$ in the

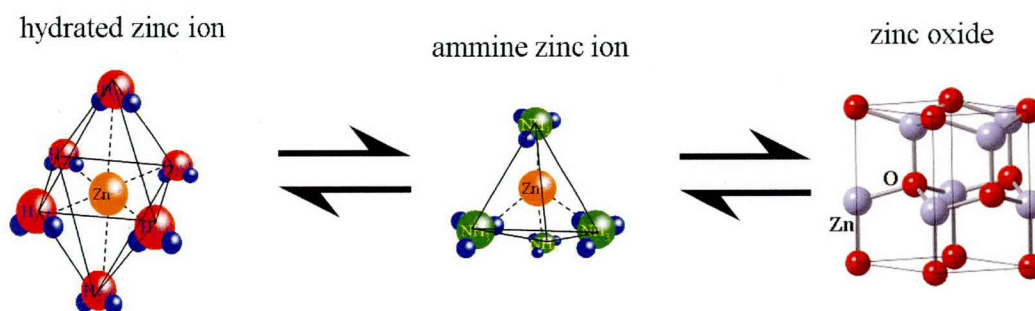


Fig. 4.4 Schematic image of equilibrium state of zinc ions in growth solution and ZnO

hydrothermal growth solution increased twice and three times, indicating that the growth rate can be controlled by altering the concentration of the Zn source. The growth rate of ZnO-E2 in the c-axis direction is similar to that of ZnO-W1. However, the morphology of the ZnO-E2 film is quite different from that of the ZnO-W1 film. The interstices between nanorods are filled in the case of the ZnO-E2 film, suggesting that crystal growth in the *a* and *b* direction for the ZnO-E2 film is faster than the ZnO-W1 film. These results indicate that the growth rate of a-axis direction against the c-axis direction can be changed by using ethanol/water mixed solvents, which resulted

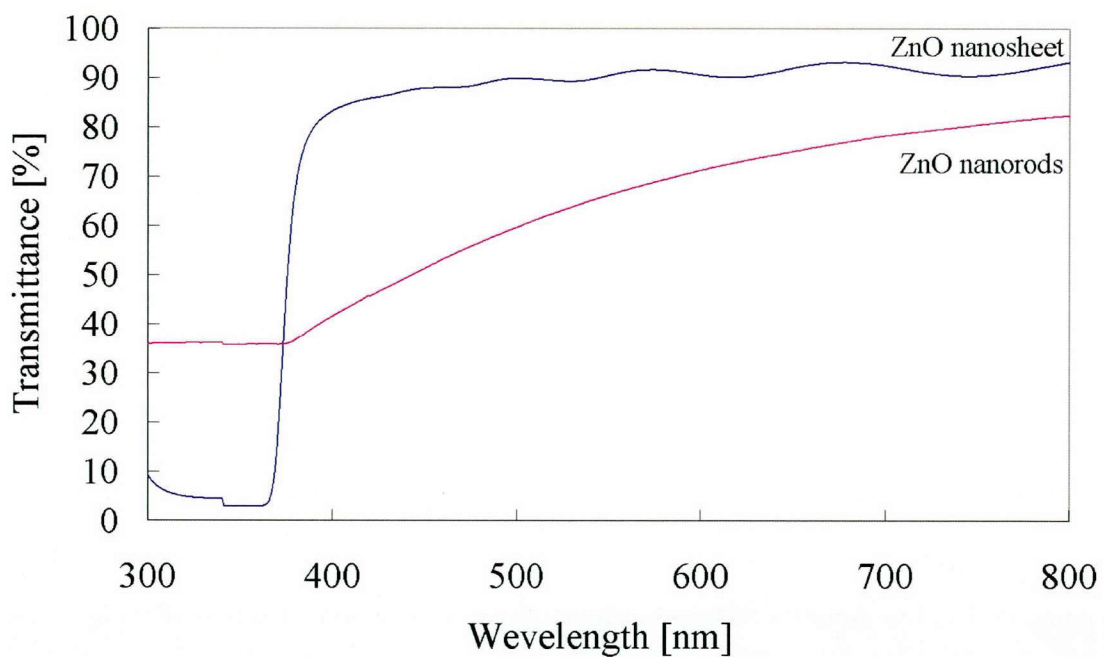


Fig. 4.5 UV-vis spectra of the ZnO-E1 film and the ZnO-W1 film

in a morphological control of ZnO films.

Fig. 4.5 shows UV-vis spectrum of the ZnO-E1 and ZnO-W1 films. The transparency of the ZnO-E1 film is up to 94% near the wavelength of 800 nm. The transparency of the ZnO-W1 film is very low because its rough surface of the film scatters a visible light. The high transparency of the ZnO-E1 film can be explained by the flat surface of the nanosheet, which can prevent a scattering of light.

Electric resistivity of the ZnO-E1 film in the direction parallel to the film surface was 25.7 Ω cm. On the other hand, the resistivity of ZnO-W1 nanorods was too large to measure because of the

presence of interstices between ZnO rods. The conductivity of the film parallel to the film surface could be improved by controlling the morphology of ZnO. Furthermore, the resistivity of nanosheet can be reduced to $4.5 \Omega \text{ cm}$ by doping Al in ZnO nanosheet (AZO-E1). It can be recognized from XRD patterns in **Fig. 4.3** that the *c*-axis orientation of nanosheet was not affected by the doping of Al.

4.4 Conclusion

In conclusion, we have successfully synthesized ZnO nanosheet which has a flat surface, *c*-axis orientation, high transparency and conductivity. The growth rate of each crystal plane of ZnO was affected by adding ethanol to growth solution. The transparent and conductive nanosheet-like ZnO and AZO films could be hydrothermally synthesized at low temperature without using seed crystals.

References

- [1] Ohta H, Kawamura K-I, Orita M, Hirano M, Sarukura N, Hosono H. Appl Phys Lett 2000;77:475.
- [2] Arnold S M, Avouris P, Pan Z W, Wang Z L. J Phys Chem B 2003;107:659.
- [3] Lee J Y, Choi Y S, Kim J H, Park M O, Im S. Thin Solid Films 2002;403:553.
- [4] Pan Z, Wang Z L, Comini E, Faglia G, Sberveglieri G. Appl Phys Lett 2002;81:1869.
- [5] Selvan J A, Keppner H, Shah A. Mater Res Soc Symp Proc 1996;426:497.
- [6] Ritala M, Asikainen T, Leskela M, J. Skarp J Mater Res Soc Symp Proc 1996;426:513.
- [7] Gupta V, Mansingh A. J Appl Phys 1996;80:1063.
- [8] Bertolotti M, Laschena M V, Rossi M, Ferrari A, Qian L S, Quaranta F, Valentini A. J Mater Res 1990;5:1929.
- [9] Weibenrieder K-S, MuÈller J. Thin Solid Films 1997;300:30.
- [10] Deschanvres J L, Bochu B, Joubert J C. J Phys 1993;4:485.
- [11] Hayamizu S, Tabata H, Tanaka H, Kawai T. J Appl Phys 1996;80:787.
- [12] Szyszka B, JaÈger S. J Non-Cryst Solids 1997;218:74.
- [13] Nakada T, Murakami N, Kunioka A. Mater Res Soc Symp Proc 1996;426:411.
- [14] Aranovich J, OrtõAz A, Bube R H. J Vac Sci Technol 1979;16:994.
- [15] O'Brien P, Saeed T, Knowles J. J Mater Chem 1996;6:1135.
- [16] Nishio K, Miyake S, Sei T, Watanabe Y, Tsuchiya T. J Mater Sci 1996;31:3651.
- [17] Ueno N, Maruo T, Nishiyama N, Egashira Y, Ueyama K. Mater Lett 2010;64:513.

Chapter 5

Synthesis of mesoporous ZnO, AZO, and BZO transparent conducting films using nonionic triblock copolymer as template

Mesoporous zinc oxide (ZnO), Al-doped ZnO (AZO) and B-doped ZnO (BZO) thin films were synthesized by a sol-gel method using nonionic triblock copolymer (Pluronic F127: EO₁₀₆PO₇₀EO₁₀₆) as a soft template agent. Electrical and optical properties of the ZnO, AZO, and BZO films were investigated. Mesoporous ZnO films calcined at 500°C showed a strong peak in the XRD pattern, showing a periodic distance of 12.8 nm. The visible light transmittance of the films was ranged from 50% to more than 90% by changing the Zn/EO molar ratio in precursor solutions. The electric resistivity of the films was decreased by doping the optimum amount of Al or B atom. The minimum value of the BZO film was 0.024 Ωcm which can be obtained at the atomic ratio of B/Zn = 0.005.

5.1 Introduction

Transparent conducting oxide layers have been extensively studied because of their broad range of applications such as transparent electrodes in display and in photovoltaic devices [1,2]. ZnO is a promising material as transparent conductor. Since ZnO is an n-type wide bandgap semiconductor, its electrical conductivity is mainly due to zinc excess at the interstitial position. Its electrical properties could be modified over several decades by an appropriate doping process.

ZnO thin films have been prepared by a variety of thin film deposition techniques, such as metal-organic chemical vapor deposition (MOCVD) [3], pulsed laser deposition [4], RF magnetron sputtering [5], chemical vapor deposition [6], spray pyrolysis [7] and sol-gel process [8], etc. But these gas phase approaches generally require highly sophisticated equipment, expensive single-crystalline substrates for oriented growth, and often face other limitations in

terms of sample uniformity and low product yield [9]. On the other hand, the sol-gel technique offers the possibility of preparing a small as well as large-area coating of ZnO thin films at low cost for technological applications.

The conductivity of ZnO is enhanced by increasing the surface area of ZnO because a concentration of oxygen vacancy near the surface contributes to carrier concentration of ZnO. Thus, porous ZnO is an attractive as a conductor. However, there have been few reports on the synthesis of porous ZnO films.

On the other hand, ordered mesoporous silica films with different nanostructures have been synthesized by a soft-template method [10, 11, 12]. In this study, the soft-template method was applied to the synthesis of porous ZnO, Al-doped ZnO (AZO) and B-doped ZnO (BZO) thin films. The molar ratios of Zn, Al, B and a soft template in precursor solutions were optimized to obtain highly-transparent films with a high electronic conductivity.

5.2 Experiment

5.2.1 Synthesis of mesoporous ZnO films

We used zinc acetate dehydrate ($\text{Zn}(\text{OAc})_2$) as zinc sources. Aluminum nitrate ($\text{Al}(\text{NO}_3)_3$) and boric acid (H_3BO_3) were used as Al and B sources which will be contained in ZnO films as impurities in order to improve the conductivity. Porous ZnO films were prepared on a silicon wafer and a quartz plate which were cut into 2×2 cm pieces. Nonionic poly-(ethylene oxide)-poly(propylene oxide)-poly (ethylene oxide) amphiphilic triblock copolymer ($\text{EO}_{106}\text{PO}_{70}\text{EO}_{106}$; Pluronic F127) was used as a templating agent. The film was deposited on the substrates by spin-coating using a mixture of $\text{Zn}(\text{OAc})_2$, surfactant, ethanol (EtOH), and deionized water. The sample names of the ZnO, AZO and BZO films and the mole ratios of the precursor solution are listed in Table 1. The film was calcined at 500°C in air for 3 h with a heating rate of 1°C/min to remove the template.

Table 5.1 Molar ratio of precursor solutions, transparency and resistivity of the films

		Molar ratio of precursor solutions					Zn/ EO*	Transmittance at 550 nm [%]	Resistivity [Ω cm]
	Zn(OAc) ₂	Pluronic F127	H ₂ O	EtOH	Al(NO ₃) ₃	H ₃ BO ₃			
ZnO-1	2.5	0.08	330	175			0.15	99.20	0.859
ZnO-2	5						0.29	99.54	0.701
ZnO-3	7.5						0.44	99.20	0.581
ZnO-4	10						0.59	84.99	0.830
ZnO-5	12.5						0.74	90.18	0.890
ZnO-6	15						0.88	74.93	0.641
ZnO-7	20						1.18	60.59	1.32
AZO-1	10	0.08	330	175	0.05		0.59	67.94	0.113
AZO-2	10				0.1		0.59	83.09	0.080
AZO-3	10				0.15		0.59	75.95	1.44
AZO-4	10				0.2		0.59	70.30	2.30
BZO-1	10	0.08	330	175		0.05	0.59	71.53	0.017
BZO-2	10					0.1	0.59	89.49	0.400
BZO-3	10					0.15	0.59	88.33	0.304
BZO-4	10					0.2	0.59	91.44	1.89
BZO-5	7.5					0.038	0.44	99.23	0.024

*One F127 molecule contains 212 EO groups.

5.2.2 Characterization

The films were identified by X-ray diffraction (XRD) patterns recorded on a Philips X'Pert-MPD using Cu-K α radiation with $k = 1.5418$ Å in the θ -2 θ Bragg-Brentano scan mode.

FE-SEM images were recorded on a Hitachi S-5000 L microscope at an acceleration voltage of 21 kV. No coating was carried out for the samples before the FE-SEM measurements.

The transparencies of the 2×2 cm ZnO films were investigated by ultra violet-visible absorbance measurement (UV-vis: Jasco V-570 UV/VIS/NIR spectrophotometer) in transmittance mode.

The electrical resistivity in the direction parallel to the film surface was measured by a four probe method using RT-70V/RG-5 Napson four-point probe.

5.3 Results and Discussion

Figs. 5.1 and 5.2 show the XRD pattern and FE-SEM images of the ZnO-4 film on a Si substrate. A strong peak is observed at $2\theta = 0.69^\circ$, which indicates that ZnO-4 film has a periodic structure with the d -space of 12.8 nm. A polycrystalline thin film with a thickness of 250 nm is observed in the FE-SEM image. The grain size was 10-15 nm which is corresponding to the d -space calculated from the XRD peak. The pore size seems to be smaller than the grain size.

However, as shown in Fig. 5.2, the porous ZnO film did not have a highly-ordered periodic structure. –In **Fig. 5.3**, a possible formation mechanism of the mesoporous ZnO was compared with that of the mesoporous silica. In the case of mesoporous silica, amorphous silica is formed around the aggregation of Pluronic F127 molecules through the condensation of Si-OH. Even after a decomposition of Pluronic F127 molecules, a periodic mesostructure was retained [12]. On the other hand, ZnO pore wall are formed through a crystallization from $\text{Zn}(\text{OAc})_2$ without through a condensation process. The ZnO pore wall deforms during crystallization even though

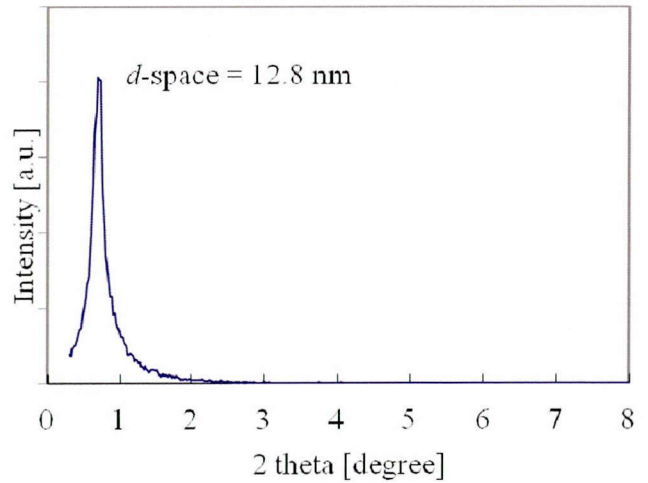


Fig. 5.1 XRD pattern of the ZnO-4 film.

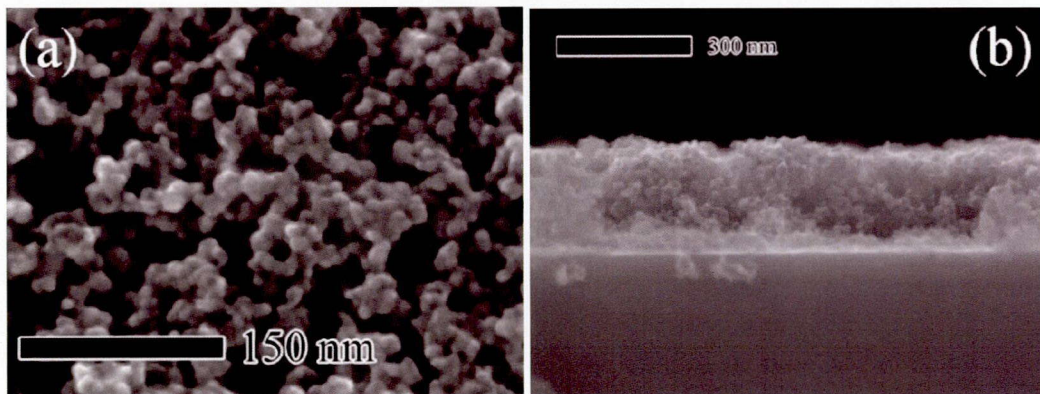


Fig. 5.2 FE-SEM images of (a) the surface and (b) the cross-section of the ZnO-4 film.

uniform mesopores are maintained. As a result, the periodic structure could have partly collapsed during the decomposition of Pluronic F127 molecules. However, large ZnO crystals were not formed because the crystal overgrowth was depressed in the presence of Pluronic F127 molecules. Thus, the pore walls were composed of ZnO polycrystals.

The polycrystalline structure seems to have a negative effect on the conductivity of the ZnO film.

However, the electronic resistivity of the ZnO-4 film was $0.83 \Omega\text{cm}$ which is lower than the reported values of the resistivity for the hydrothermally-synthesized ZnO nanorod [13] and nanosheet films ($>25.7 \Omega\text{cm}$) [14]. The low resistivity could be derived from the increase of the concentration of oxygen vacancy in porous ZnO film with a high surface area. The effect of interaction between Zn ions and Pluronic F127 molecules on the formation of ZnO in alkaline solution was discussed by Li et al. [15] who prepared ZnO powder in the presence of Pluronic

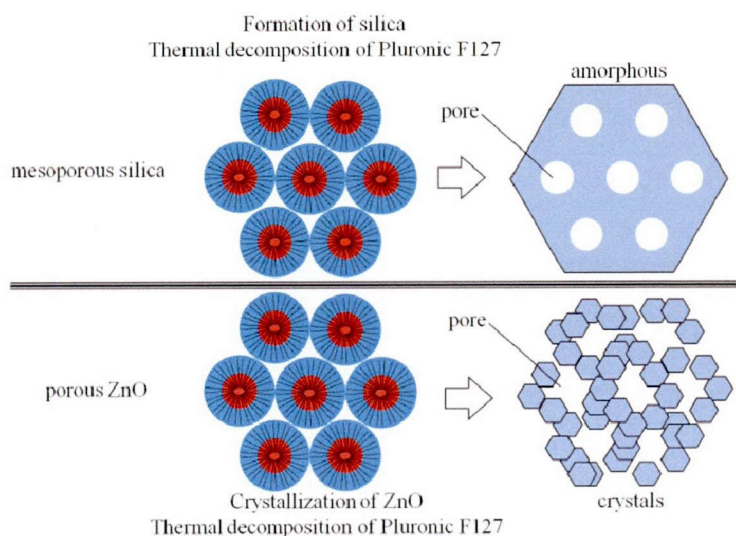


Fig. 5.3 A formation mechanism of mesoporous silica and porous ZnO films.

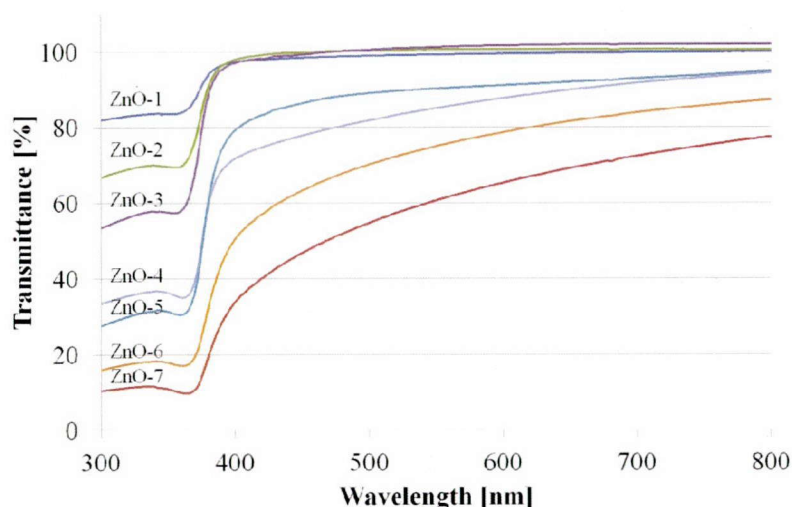


Fig. 5.4 UV-Vis spectra of the porous ZnO films synthesized at different concentrations of Zn in the precursor solutions.

F127. They reported that a replacement of coordinated water molecule by OH is restrained in the presence of Pluronic F127 due to the hydrogen bond that is formed between coordinated water molecule and the hydrophilic chains of Pluronic F127. Under such conditions, only part of the water molecules coordinated with

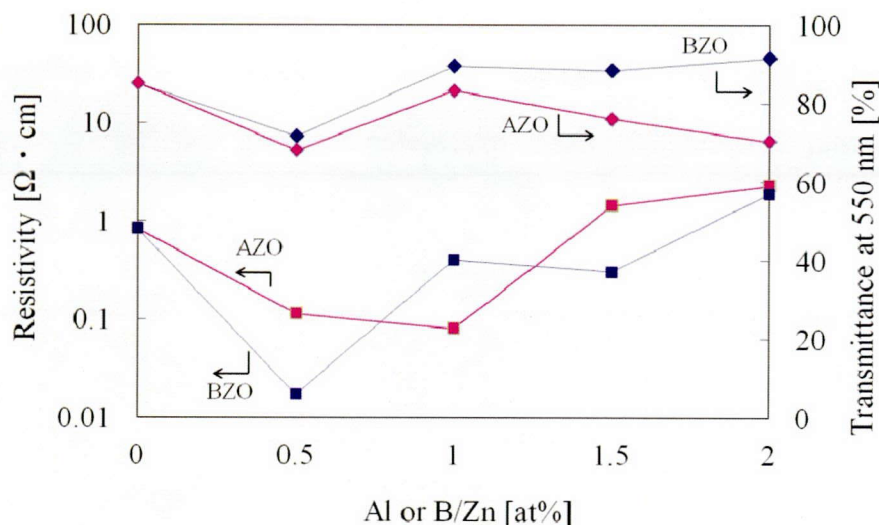


Fig. 5.5 The resistivity and transmittance of the porous AZO and BZO films.

Zn^{2+} would be replaced with an OH^- group. Nearly the same phenomena could occur in Zn^{2+} and oxygen under heating in this case. As mentioned above, the water molecules coordinated with Zn^{2+} would be replaced with oxygen, which resulted in the increase of the

concentration of oxygen vacancy.

Fig. 5.4 shows the UV spectra of the mesoporous ZnO films synthesized using the solutions with different Zn concentrations. The visible light transmittance of the mesoporous ZnO-1, 2 and 3 films is nearly 100% at the wavelength of 550 nm. Their visible light transmittance decreased when the concentration of Zn in precursor solutions was higher than 12.5 M (ZnO-4 ~ ZnO-7). The opacity of the ZnO-4 ~ ZnO-7 films can be observed visually.

It is reported that Pluronic F127 molecules can thermodynamically stabilize the $\text{Zn}(\text{H}_2\text{O})_6^{2+}$ unit cell by the hydrogen bond interaction between Pluronic F127 hydrophilic chains (EO groups) and the water molecule.[15] In our study, the molar ratios of Zn/EO in the solution were 0.15~1.18 as listed in Table 1. The transparency decreased when the Zn/EO molar ratio is higher than 0.59 (ZnO-4). These results suggest that one $\text{Zn}(\text{H}_2\text{O})_6^{2+}$ ion can interact with two EO groups of the Pluronic F127 molecule. Particles with different sizes were

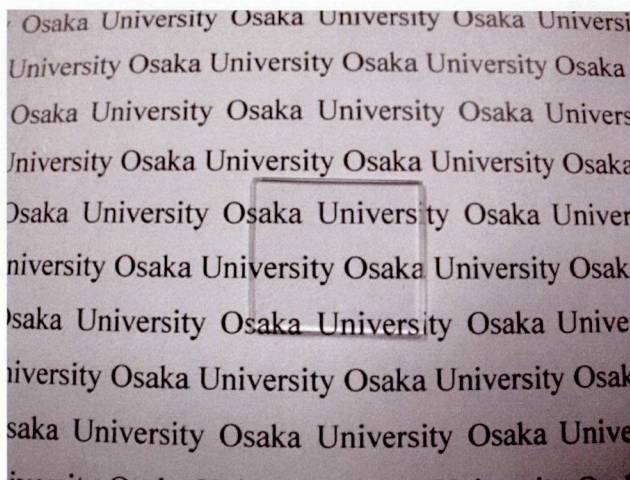


Fig. 5.6 The photograph of the porous BZO-5 film on the quartz substrate.

observed on the non-transparent films (ZnO-5 ~ ZnO-7) from SEM images (Data not shown). Large particles can be simultaneously formed from excess Zn ions which did not interact with Pluronic F127 molecules.

Fig. 5.5 shows the resistivity and transmittance of Al and B-doped porous ZnO films (AZO and BZO films) as a function of the doping ratios of Al/Zn and B/Zn.. The AZO and BZO films show nearly the same transparency as the no-doped porous ZnO films, which indicate that the transparency of the films is not affected by the doping ratios of Al and B. On the other hand, the resistivity of the films attained a minimum value with increasing the doping ratios. The AZO-2 and BZO-1 film showed 10 and 40 times higher conductivities than the no-doped ZnO-4 film, respectively. According to Dai *et al.* [16], Al atoms in the AZO films are substituted in the Zn site when the content of Al₂O₃ is lower than 5 wt%. The spare electrons from Al can improve the conductivity of AZO significantly. Beyond 5 wt%, an independent Al₂O₃ crystal phase (insulator) appears, leading to the increase of the resistivity. The AZO-2 film in this study shows the minimum value of electrical resistivity (0.080Ωcm) in the AZO films. These facts demonstrate that the Al atom was doped into AZO films and contributes to the improvement of the conductivity.

Finally, a highly-conductive transparent BZO film was synthesized on a quartz substrate using optimized synthetic conditions (BZO-5). A photograph of the BZO-5 film was shown in **Fig. 5.6**. The film shows both high transparency and high conductivity. The visible light transmittance of the BZO-5 film showed more than 90% at the wavelength of 550 nm. The resistivity was 0.024 Ωcm which was the lowest value in this study.

5.4 Conclusion

Porous ZnO thin films were synthesized by applying the soft template method. The films thickness was about 250 nm. The ZnO films were composed of ZnO grains with a size of 10-15 nm. The ZnO films show resistivities lower than the hydrothermally-synthesized ZnO nanorod and nanosheet films possibly because of the high concentration of oxygen vacancy on the pore surface and their high surface area. The lowest resistivity value (= 0.024Ωcm) was achieved at the atomic ratio of B/Zn = 0.005. The optical transmittance was higher than 90% and the surface morphologies of the films were uniform when the molar ratio of Zn ion/EO group was lower than 0.5.

References

- [1] Chen M, Pei ZL, Sun C, Gong J, Huang RF, Wen LS. *Mater Sci Eng B* 2001;85:212-7.
- [2] Herero J, Gutierrez MT, Guillen C, Dona JM, Martinez MA, Chaparro AM, Bayon R. *Thin Solid Films* 2000;361:28-33.
- [3] Fang X, Li J, Zhao D, Shen D, Li B, Wang X. *J Phys Chem C* 2009;113:21208-12.
- [4] Sub E, Kang SHS, Kang JS, Kim JH, Lee SY. *Appl Surf Sci* 2002;186:474-6.
- [5] Nunes P, Costa D, Fortunato E, Martins R. *Vacuum* 2002;64:293-7.
- [6] Kashiwaba Y, Katahira F, Haga K, Sekiguchi T, Watanabe H. *J Crystal Growth* 2000;221:431-4.
- [7] Paraguay FD, Estrada WL, Acosta DR, Andrade E, Miki-Yoshida M. *Thin Solid Films* 1999;350:192-202.
- [8] Kamalasanan MN, Chandra S. *Thin Solid Films* 1996;288:112-5.
- [9] Strikant V, Clark DR. *J Mater Res* 1997;12:1425-8.
- [10] Murakami Y, Yamakita S, Okubo T, Maruyama S. *Chem. Phys Lett* 2003;375:393-8.
- [11] Hillhouse HW, Egmond JW, Tsapatsis M. *Chem Mater* 2000;12:2888-93.
- [12] Nishiyama N, Tanaka S, Egashira Y, Oku Y, Ueyama K. *Chem Mater* 2002;14:4229-34
- [13] Ueno N, Maruo T, Nishiyama N, Egashira Y, Ueyama K. *Mater. Lett.* 2012;64:513–5
- [14] Ueno N, Yamamoto A, Uchida Y, Egashira Y, Nishiyama N. *Mater. Lett.* 2012;86:65–8
- [15] Li H, Zhang Y, Wang J. *J Am Ceram Soc* 2012;95:1241-6
- [16] Dai HQ, Xu H, Zhou YN, Lu F, Fu ZW. *J Phys Chem C* 2012;116:1519-25

Chapter 6

Summary

6.1 Summary

6.1.1 Synthesis of Zinc Oxide Nanorods Films using Zn/SDS Composite

In chapter 2, the zinc oxide nanorods film using zinc/SDS composite films were synthesized by the hydrothermal synthesis. The zinc oxide nanorods films could be synthesized from the zinc/SDS composite seed without using any crystal seeds at low temperature. The composite formed a layered structure. A uniform nanorods film could be formed because the highly-dispersed zinc molecules effectively assisted the nucleation of zinc oxide crystals under hydrothermal conditions even at low temperature. This result was the first example to synthesize a highly ordered zinc oxide nanorods films by a low temperature hydrothermal method.

6.1.2 Formation Mechanism and Control of Zinc Oxide Nanorods Films

In chapter 3, the formation mechanism and control of zinc oxide nanorods films were studied. The reaction conditions of hydrothermal synthesis such as composition, temperature, heating time, stirring rate and batch or continuous flow were changed in order to control the morphology of zinc oxide. The composition and stirring rate of growth solution had a strong effect on the aspect ratio of nanorods. Homogeneous nucleation proceeded in the growth solution with a rise of temperature. At the same time, zinc in Zn/SDS composite reacted to form zinc oxide. The growth of zinc oxide nanorods on the substrate started after the growth solution reaches quasi-equilibrium state.

6.1.3 Synthesis of Zinc Oxide Nanosheet Films using Zn/SDS Composite

In chapter 4, zinc oxide nanosheet films were synthesized by using ethanol as a solvent. When the alcohols are used as a solvent, the nucleation density of zinc oxide on the substrate and in the solvent was decreased compared with that in the water. The zinc oxide nanosheet synthesized with ethanol as a solvent had a flat surface and high transparency. In addition, the nanosheet had higher conductivity than that of the nanorods films. The conductivity could be controlled even higher when the Al atoms are doped in the zinc oxide crystal structure,

6.1.4 Synthesis of Porous Zinc Oxide Films using Zn/F127 Composite

In chapter 5, the porous zinc oxide films were synthesized using a triblock copolymer Pluronic F127 as a template. The transparency and conductivity of porous zinc oxide films were higher than that of zinc oxide nanosheet. The films had a flat surface. The structure of the films seems to be nearly the same as that of the Zn/F127 composite. The high conductivity of the films could be derived from the increase of the carrier concentration because the oxygen defect which is the carrier of zinc oxide localized in the vicinity of the crystal surface increased with the increase of the surface areas of zinc oxide. Doping of Al and B atoms derived higher conductivity, which was also caused by the increase of carrier concentration.

List of Publications

Papers

1. “Low-temperature synthesis of ZnO nanorods using a seed layer of zinc acetate/sodium dodecyl sulfate nanocomposite” N. Ueno, T. Maruo, N. Nishiyama, Y. Egashira, Korekazu Ueyama *Materials Letters* 64 (2010) 513–515
2. “Low-temperature synthesis of ZnO nanorods using organic–inorganic composite as a seed layer” N. Ueno, K. Nakanishi, T. Ohta, Y. Egashira, N. Nishiyama *Thin Solid Films* 520 (2012) 4291–4296
3. “Low-temperature hydrothermal synthesis of ZnO nanosheet using organic/inorganic composite as seed layer” N. Ueno, A. Yamamoto, Y. Uchida, Y. Egashira, N. Nishiyama *Materials Letters* 86 (2012) 65–68

Related paper

1. “Transmission electron microscopy study on the growth of zinc oxide crystals under hydrothermal conditions” T. Maruo, N. Ueno, S. Ichikawa, N. Nishiyama, Y. Egashira, K. Ueyama *Materials Letters* 63 (2009) 2373–2376

Proceedings

1. “Synthesis of oriented zinc oxide films by low-temperature hydrothermal method” Naoyuki Ueno, Yoshiaki Uchida, Yasuyuki Egashira, Norikazu Nishiyama, 10th Japan-Korea Symposium on Materials and Interfaces, Kyoto, Japan 2012

Acknowledgements

I would like to thank my supervisors Prof. Dr. Norikazu Nishiyama, Associate Prof. Dr. Yasuyuki Egashira, and Associate Prof. Dr. Yoshiaki Uchida (Division of Chemical Engineering, Graduate school of Engineering Science, Osaka University) for their contributions to this work. With their guidance I have been able to push my research to proceed and yet to keep on right track.

I extremely appreciate my supervisor, Prof. Dr. Norikazu Nishiyama. I am really indebted to you for helping me advance my research actively. Your critical comments on the manuscripts of my papers are gratefully acknowledged.

Associate Prof. Dr. Yasuyuki Egashira, I am indebted to your kind helps and suggestions. Your attitude towards science impressed me deeply. I was lucky to have opportunity to hear your thoughts about coverall science.

Assistant Prof. Dr Yoshiaki Uchida is acknowledged for giving me constructive comments and warm encouragement.

I deeply appreciate emeritus Prof. Korekazu Ueyama. His sttitude towards research impressed me deeply. I wish to acknowledge my gratitude to Prof. Dr. Michio Matsumura and Prof. Dr. Takayuki Hirai (Research Center for Solar Energy Chemistry, Osaka University) for the critical comments and helpful suggestions on my dissertation. I am thankful to Mr. Masao Kawashima (GHAS laboratory, Division of Chemical Engineering, Osaka University) for the FE-SEM measurements. I gratefully thank Dr. Satoshi Ichikawa (Organization for the Promotion of Research on Nanoscience and Nanotechnology, Osaka University) for the TEM measurements and giving advice of future career. I acknowledge the center of excellence (21COE) program "Creation of Integrated EcoChemistry" and the Global Centers of Excellence (GCOE) program "Global Education and Research Center for Bio-Environmental Chemistry" of Osaka University.

Thanks are given to my coworkers, Dr. Takanori Maruo, Mr. Shigekazu Tanaka, Mr. Daiki Ushigome, Mr. Morales Guio Carlos Gilberto, Mr. Akinobu Yamamoto and Mr. Bram Dwijaya for their nice circumstances. Special thanks are given to Dr. Yuko Nishiyama

(current last name is Maruo), Dr. Yong-Rong Dong, Dr. Vu Van Dung, Dr. Jin Jin and Dr. Yuichiro Hirota for all their help, support, interest and valuable advices. It is a pleasure to thank Mr. Shinji Ejiri, Mr. Masaki Taniyama, Ms. Kaori Midoumaru, Mr. Kenji Murata, Mr. Hiroki Yoshii, Mr. Yuichi Nakano, Mr. Takahito Mitome, Mr. Yousuke Iwai, Ms. Anna Shinmura, Mr. Tatsuya Matsumoto, and Mr. Yusuke Sugiura and all present and former colleagues in Nishiyama Laboratory for a lot of nice talks about private matters during break time. I am also indebted to many others whose names could not be mentioned here for space reasons for their kindness and pleasant time. I wish to express my thanks to my best friends, Mr. Takuya Minami, Mr. Hitoshi Fukui, Mr. Atsushi Sato and Mr. Takashi Uesugi. I could not keep up this work without their encouragement.

Finally, I would like to thank my wife Eri, my daughter Aki, my father Seiji, my mother Takako, my brother Yasuhiro, my sister Hiroko, my grandfather Harukichi and my grandmother Yoshiko and Kazuko for their understanding and incredible support.

Naoyuki Ueno

Osaka, Japan

March 2013

